

# **Thermal Aspects and Electrolyte Mass Transport in Lithium- ion Batteries**

HENRIK LUNDGREN

Doctoral Thesis, 2015  
KTH Royal Institute of Technology  
School of Chemical Science and Engineering  
Department of Chemical Engineering and Technology  
Applied Electrochemistry  
SE-100 44 Stockholm, Sweden

© Henrik Lundgren 2015

TRITA CHE REPORT 2015:22

ISSN 1654-1081

ISBN 978-91-7595-584-1

Akademisk avhandling som med tillstånd av KTH i Stockholm framlägges till  
offentlig granskning för avläggande av teknisk doktorsexamen 11 juni kl. 10:00 i  
sal D2, KTH, Lindstedtsvägen 5, Stockholm.

## **Abstract**

Temperature is one of the most important parameters for the performance, safety, and aging of lithium-ion batteries and has been linked to all main barriers for widespread commercial success of electric vehicles.

The aim of this thesis is to highlight the importance of temperature effects, as well as to provide engineering tools to study these.

The mass transport phenomena of the electrolyte with LiPF<sub>6</sub> in EC:DEC was fully characterized in between 10 and 40 °C and 0.5 and 1.5 M, and all mass transport properties were found to vary strongly with temperature.

A superconcentrated electrolyte with LiTFSI in ACN was also fully characterized at 25 °C, and was found to have very different properties and interactions compared to LiPF<sub>6</sub> in EC:DEC.

The benefit of using the benchmarking method termed electrolyte mass-transport resistivity (EMTR) compared to using only ionic conductivity was illustrated for several systems, including organic liquids, ionic liquids, solid polymers, gelled polymers, and electrolytes containing flame-retardant additives.

TPP, a flame-retardant electrolyte additive, was evaluated using a HEV load cycle and was found to be unsuitable for high-power applications such as HEVs.

A large-format commercial battery cell with a thermal management system was characterized using both experiments and a coupled electrochemical and thermal model during a PHEV load cycle. Different thermal management strategies were evaluated using the model, but were found to have only minor effects since the limitations lie in the heat transfer of the jellyroll.

## **Keywords**

Energy storage, Lithium-ion batteries, Electrolytes, Temperature, Modeling, Hybrid electric vehicle, Plug-in hybrid electric vehicle

## **Sammanfattning**

Temperatur är en av de viktigaste parametrarna gällande ett litiumjonbatteris prestanda, säkerhet och åldring och har länkats till de främsta barriärerna för en storskalig kommersiell framgång för elbilar.

Syftet med den här avhandlingen är att belysa vikten av temperatureffekter, samt att bidra med ingenjörsverktyg att studera dessa.

Masstransporten för elektrolyten  $\text{LiPF}_6$  i EC:DEC karakteriseras fullständigt i temperaturintervallet 10 till 40 °C för  $\text{LiPF}_6$ -koncentrationer på 0.5 till 1.5 M. Alla masstransport-egenskaper fanns variera kraftigt med temperaturen.

Den superkoncentrerade elektrolyten med LiTFSI i ACN karakteriseras även den fullständigt vid 25 °C. Dess egenskaper och interaktioner fanns vara väldigt annorlunda jämför med  $\text{LiPF}_6$  i EC:DEC.

Fördelen med att använda utvärderingsmetoden elektrolytmasstransportresistivitet (EMTR) jämfört med att endast mäta konduktivitet illustreras för flertalet system, däribland organiska vätskor, jonvätskor, fasta polymerer, gellade polymerer, och elektrolyter med flamskyddsadditiv.

Flamskyddsadditivet TPP utvärderades med en hybridbils-lastcykel och fanns vara olämplig för högeffektsapplikationer, som hybridbilar.

Ett kommersiellt storformatsbatteri med ett temperatur-kontrollsyste姆 karakteriseras med både experiment och en kopplad termisk och elektrokemisk modell under en lastcykel utvecklad för plug-in-hybridbilar. Olika strategier för kontroll av temperaturen utvärderades, men fanns bara ha liten inverkan på batteriets temperatur då begränsningarna för värmetransport ligger i elektrodrullen, och inte i batteriets metalliska ytterhölje.

## List of appended papers

### Paper I

Impact of the flame retardant additive triphenyl phosphate (TPP) on the performance of graphite/LiFePO<sub>4</sub> cells in high power applications.  
Katarzyna Ciosek Högström, Henrik Lundgren, Susanne Wilken, Tommy Zavalis, Mårten Behm, Kristina Edström, Per Jacobsson, Patrik Johansson and Göran Lindbergh.

*Journal of Power Sources* **256**, 430-439 (2014)

### Paper II

Electrochemical Characterization and Temperature Dependency of Mass-Transport Properties of LiPF<sub>6</sub> in EC:DEC.  
Henrik Lundgren, Mårten Behm and Göran Lindbergh.

*Journal of the Electrochemical Society* **162** (3), A413-A420 (2015)

### Paper III

Characterization of the Mass-Transport Phenomena in a Superconcentrated LiTFSI:Acetonitrile Electrolyte.  
Henrik Lundgren, Johan Scheers, Mårten Behm and Göran Lindbergh.

*Journal of the Electrochemical Society* **162** (7), A1334-A1340 (2015)

### Paper IV

Electrolyte Mass-Transport Benchmarking of Four Types of Lithium-Ion Battery Electrolytes: Organic liquids, Ionic Liquids, Gelled Polymers, and Solid Polymers.

Henrik Lundgren, Mårten Behm and Göran Lindbergh.

*Manuscript*

### Paper V

Thermal Management of Large-Format Prismatic Lithium-Ion Battery in PHEV Application.

Henrik Lundgren, Pontus Svens, Henrik Ekström, Carl Tengstedt, Johan Lindström, Mårten Behm and Göran Lindbergh.

*Submitted to the Journal of the Electrochemical Society*

The appended papers were collaborations with the co-authors, and I did not contribute to all parts of the papers. In Paper I, K.C. Högström was responsible for full-cell testing, scanning electron microscopy, and the X-ray photoelectron spectroscopy; and S. Wilken was responsible for the Raman spectroscopy, viscosity measurements, and the DFT calculations. In Paper II, S. Wilken was responsible for the density and viscosity measurements. In Paper III, J. Scheers was responsible for the density and viscosity measurements. In Paper V, the model was developed together with H. Ekström, the electrochemical testing performed together with P. Svens, and the scanning electron microscopy measurements together with C. Tengstedt.

## Doktor Henriks Session IPA

**Bryggvolym:** 30 L

**OG:** 1.045      **FG:** 1.011  
**ABV:** 4.5%      **IBU:** 41



### Malt:

4.7 kg Pale ale-malt  
1.0 kg Ljus vetemalt  
0.3 kg Vete-karamellmalt

### Jäst:

California Ale (Whitelabs WLP001)

### Humle:

200 g Equinox (13.9 % α-syra)  
100 g Simcoe (12.3 % α-syra)

### Mäskningsschema

Steg	Tid	Temperatur
Försockringsrast	60 min	65 °C
Utmäskning	1 min	78 °C

### Vörtkok

Koktid	Humle #1	mängd	Humle #2	mängd
60 min	Equinox	5 g	Simcoe	5 g
20 min	Equinox	10 g	Simcoe	20 g
10 min	Equinox	45 g	Simcoe	15 g
0 min	Equinox	40 g	Simcoe	20 g

1 g Protafloc tillsättes 15 min före kokets slut

### Jäsning

Steg	Tid	Temperatur
Primärjäsning	14 dagar	20 °C
Sekundärjäsning	14 dagar	20 °C

### Torrhumling

30 g Simcoe och 40 g Equinox vid sekundärjäsningens början, 10 g Simcoe och 60 g Equinox 7 dagar senare.



# Table of Contents

<b>Chapter 1: Introduction</b>	<b>1</b>
1.1 Lithium-ion batteries	1
1.2 Effect of temperature	3
1.3 Electrolytes	4
1.4 Safety	6
1.5 Aim of this thesis	8
<b>Chapter 2: Methods</b>	<b>9</b>
2.1 Materials	9
2.2 Experimental	10
2.3 Modeling	15
2.3.1 Electrolyte model	15
2.3.2 Full cell model	17
2.3.3 Thermal model	18
2.4 Optimization	20
<b>Chapter 3: Results and discussion</b>	<b>23</b>
3.1 Electrolyte characterizations	23
3.1.1 Density, viscosity, and partial molar volumes	23
3.1.2 Ionic conductivity	27
3.1.3 Diffusion coefficient, transport number, and thermodynamic enhancement factor	30
3.1.4 Electrochemical stability	34
3.1.5 Electrolyte benchmarking using electrolyte mass transport resistivity	36
3.2 TPP Flame retardant in HEV application	38
3.3 Thermal modeling of commercial 25 Ah battery in PHEV application	40
3.4.1 Model validation	40
3.4.2 Electrochemical processes and internal thermal performance	41
3.4.3 Comparison using different electrolytes	44
<b>Chapter 4: Future work</b>	<b>47</b>
<b>Chapter 5: Conclusions</b>	<b>49</b>
<b>Chapter 6: List of symbols</b>	<b>51</b>

<b>Chapter 7: Acknowledgements</b>	<b>53</b>
<b>Chapter 8: References</b>	<b>55</b>

## Chapter 1: Introduction

Climate change and modern society have put increasing demands on humans to be more energy efficient and connected, which has led to batteries playing a larger role in our everyday lives. Batteries can be divided into two groups based on whether they are rechargeable (secondary battery) or not (primary battery). The four dominating technologies for secondary batteries are lead acid, lithium-ion, nickel metal-hydride, and nickel cadmium. High cell voltage, low self-discharge rate, and high gravimetric and volumetric energy and power density, compared to the other three types has given rise to a large increase in the market for lithium-ion batteries<sup>1</sup>. In 2009, 37 % of the total revenues of the global battery market was attributed to lithium-ion batteries<sup>2</sup>. The value of the annual lithium-ion battery market has grown incredibly, estimated to reach \$23.6 billion in 2015, from approximately \$17.5 billion in 2009<sup>3</sup>. There are some technologies being researched with a potential quantum leap in performance compared to lithium-ion batteries, e.g. lithium-sulfur and lithium-oxygen batteries, but these are far from being commercialized<sup>4,5</sup>. This thesis will focus solely on the lithium-ion battery (LIB).

### 1.1 Lithium-ion batteries

LIBs were first proposed in the 1970s<sup>6–10</sup>, and were commercialized in 1991 by Sony. LIBs are a group of batteries where lithium ions are shuttled between two host materials, and stored in the hosts' crystal structures. The host materials are called electrodes, and the electrode with the highest electrode potential is called the positive electrode, and consequently the electrode with the lowest electrode potential is called the negative electrode. The positive electrode is commonly a transition metal oxide<sup>11</sup>, such as lithium cobalt oxide or nickel manganese cobalt oxide, or a transition metal phosphate, such as lithium iron phosphate. Graphite is by far the most common negative electrode material, but other possible materials include silicon, and lithium titanate. In addition to the two electrodes, which are coated onto metal current collectors

## 2 | Chapter 1: Introduction

(commonly aluminum for the positive electrode, and copper for the negative electrode), where the electrochemical reactions take place, an electrolyte is needed transferring ions between the electrodes. The electrolyte is most commonly liquid, and consists of a lithium salt, e.g. lithium hexafluorophosphate ( $\text{LiPF}_6$ ), dissolved in solvent, normally a mixture of cyclic, e.g. ethylene carbonate (EC), and linear organic carbonates, e.g. diethyl carbonate (DEC), dimethyl carbonate (DMC) or ethyl methyl carbonate (EMC). Additionally, a separator is needed for liquid electrolytes to prevent short circuit when the cell is assembled. A schematic representation including the basic operating principle of a LIB is displayed in Figure 1.

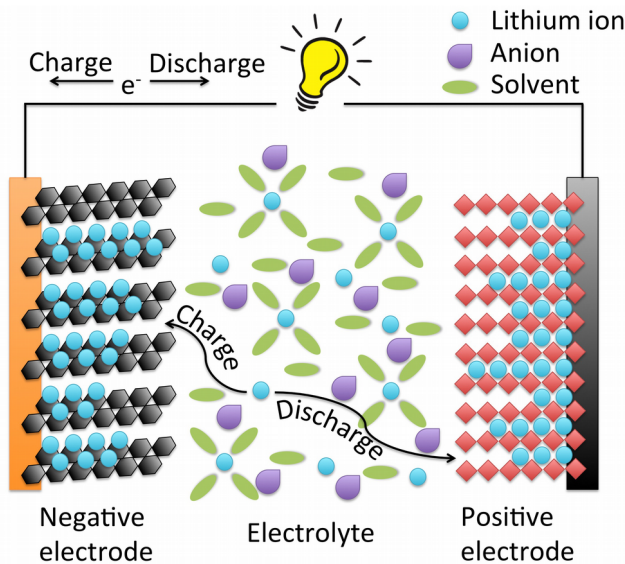


**Figure 1:** Schematic representation of a lithium-ion battery.

A typical LIB cell layer as seen in Figure 1 has a thickness of about 100–200  $\mu\text{m}$ , depending on its intended use. Applications requiring a high energy density use thicker electrodes, thus acquiring a large fractions of active material (i.e. electrodes), while applications demanding high power use thinner electrodes to ensure fast mass transport.

## 1.2 Effect of temperature

Temperature is one of the most important parameters when it comes to the performance, safety, and aging of LIBs, and has been linked to all main barriers of widespread commercial success of electric vehicles <sup>12</sup>. In the United States of America's department of energy's (USDOE) energy storage goals it is stated that the batteries of electric vehicles should be able to operate in temperatures ranging from - 30 °C to + 52 °C <sup>13</sup>. Low temperatures lead to reduced performance, and may result in the battery being unable to produce the desired electrical power. Low temperatures also increase the risk of lithium-plating on the negative electrode, which has very aggravating aging effects <sup>14</sup>, due to limitations in lithium diffusion in graphite <sup>15</sup>. Higher temperature yields faster kinetics, but not only for the desired reactions but also for the undesired side-reactions, leading to increased aging <sup>16-19</sup>. In fact, to reach the goal of 15 years calendar life set up by the USDOE for automotive batteries, strict temperature control may be needed, even during standby <sup>12</sup>.

The temperature is controlled by a thermal management system. The type of cooling used can be classified based on the type of cooling medium: air, liquid, or phase-change material. The two former are examples of active cooling, where power consuming components (i.e. pumps or blowers) are used for cooling <sup>20-24</sup>, and the latter a type of passive cooling, where the batteries are surrounded by a solid phase-change material with an appropriate melting point, thus utilizing the latent heat of melting <sup>25-27</sup>. For large-format cells, and in high-power applications, only liquid cooling can provide sufficient heat dissipation capabilities <sup>28</sup>.

The performance of the electrolyte varies strongly with temperature. Choosing the appropriate solvent mixture for liquid electrolytes is crucial if the battery is intended to be used at low temperatures, as some electrolytes will start crystallize already at 0 °C <sup>29</sup>. The electrochemical mass transport properties of the electrolyte change with temperature as well. Both the ionic conductivity and the salt diffusion coefficient have been found to increase with temperature, likely linked to a lowered viscosity <sup>29,30</sup>. The lithium-ion transport number has been found to be constant with temperature for some systems <sup>30</sup>, and increasing with

## 4 | Chapter 1: Introduction

temperature for others<sup>31</sup>, thus improving performance.

Thermal modeling can be a useful tool to study temperature effects in batteries. A thermal model consists of a thermal energy balance over the studied geometry coupled with a model for the heat generation. Heat is generated due to overpotentials, i.e. deviations from the equilibrium potential, and resistances, and is often calculated using an equation developed by Bernardi *et al.*<sup>32</sup>, and can be based on either an electrochemical model<sup>33–47</sup>, an equivalent circuit model<sup>48,49</sup>, or experimental characterizations of the relation between current and voltage at different state-of-charge (SOC)<sup>50,51</sup>.

Risks related to high temperatures are discussed in the Section on safety (Section 1.4).

### 1.3 Electrolytes

An electrolyte intended for LIBs must be electrochemically stable over a wide potential window, offer fast ion transport (especially lithium-ion transport), high lithium-ion transport number, electrically insulating, chemically and thermally stable, safe, non-toxic, environmentally benign, and cheap<sup>52</sup>. The internal ranking of this wish list is highly dependent on the intended application, and electrolytes are often tailored for its specific application.

Because of this, several different types of LIB electrolytes have been developed, including organic-solvent based, with a lithium salt dissolved in an organic solvent; ionic-liquid based, utilizing a room-temperature ionic liquid (RTIL) to dissolve the lithium salt; solid polymer based, where the lithium salt is dissolved in a polymer matrix; gelled polymers, where a lithium salt is dissolved in a polymer matrix swelled with organic solvents; and ceramic or glassy types, which are crystalline compounds with lithium incorporated in the structure. A RTIL is a salt utilizing bulky ions preventing it from crystallizing, thus being molten at room temperature. When using liquid electrolytes, i.e. organic-solvent based or ionic-liquid based electrolytes, a separator is needed to prevent short-circuit. In addition to being an extra component, with potential

compatibility problems with the different components, the separator lowers the effective mass transport properties because of its porosity and tortuosity. Table 1 summarizes some generalized characteristics of these five electrolyte types.

**Table 1:** Characteristics of different electrolyte types, where + correspond to good, and - to poor<sup>52</sup>. (T) indicate that the property is highly affected by temperature.

Electrolyte	Ionic conductivity (T)	Li <sup>+</sup> Transport number	Electrochemical window	Safety (T)
Organic liquid	+	+	-	-
Ionic liquid	+	-	-	+
Solid polymer	-	-	+	-
Gelled polymer	+	+	-	-
Ceramic	-	+	+	+

The most common type of electrolyte is organic liquids based on organic carbonates. Such solvents are not electrochemically stable at the potentials present in lithium-ion batteries, and during the first cycles a film is formed on the graphite called the solid electrolyte interphase (SEI), passivating the electrode<sup>53</sup>. Ethylene carbonate has long been regarded as a mandatory component because of its ability to form a stable SEI, and as it does not co-intercalate into graphite, as other solvents have been shown to do<sup>52,54-56</sup>. In a typical organic carbonate based electrolyte, the lithium ion is solvated by about four solvent molecules<sup>57-59</sup>, and the solvent to salt ratio is about 10:1, thus having an excess of solvent. However, it has been shown that lowering the salt to solvent ratio to the point where the lithium-ion has an incomplete solvation shell, i.e. there are not enough solvent molecules to fully solvate the lithium-ion, has positive effects on solvent co-intercalation suppression and decreases capacity fade. This is called the “solvent in salt” concept, and the

## 6 | Chapter 1: Introduction

electrolytes are considered to be superconcentrated<sup>60–65</sup>. Several different solvents have been shown to be stabilized by this concept, including dimethyl sulfoxide (DMSO), 1,2-dimethoxyethane (DME), 1,2-dioxolane (DOL), acetonitrile (ACN), and tetrahydrofuran (THF). The improved stability is believed to be due to that there are no “free” solvent molecules, i.e. all are coordinated to the ions. Superconcentrated electrolytes are almost like RTILs, and in fact the salt concentration of most studied superconcentrated electrolytes (>4 M) is higher than in normal RTILs (~3.5 – 4 M).

### 1.4 Safety

Safety risks related to LIBs have gained increasing attention. Accidents, such as the fires of the battery packs of the Boeing 787 Dreamliner<sup>66</sup>, gets a lot of media attention and generates bad publicity for LIBs. The main issue is the use of a highly flammable electrolyte in combination with a cell design aimed at maximizing the intrinsically high energy and power density. Abuse conditions, e.g. over-charging, over-heating or short-circuiting, can lead to exothermic reactions, and in the worst case thermal runaway and fire. These exothermic reactions range from oxidation/reduction of the electrolyte at the positive/negative electrode, thermal decomposition of the electrolyte, thermal decomposition of the electrodes, and possibly the melting of the separator with subsequent internal short circuit<sup>53</sup>. The situation is worsened by the fact that some positive electrode materials produce oxygen during decomposition and over-charge<sup>67,68</sup>. Safety issues are one of the main reasons for the slow implementation of hybrid electric vehicles (HEVs), plug-in hybrid electric vehicles (PHEVs), and battery electric vehicles (BEVs)<sup>69–71</sup>.

Because of these safety issues, a lot of work has been put into developing electrolytes with reduced flammability. This can be achieved by using non-flammable solvents, such as ionic liquids<sup>72,73</sup>, non-flammable electrolyte types, e.g. ceramics<sup>74</sup>, or by implementing flame-retardant additives<sup>75</sup>.

One of the flame retardant additives that was studied first was trimethyl phosphate (TMP)<sup>76</sup>. However, it was found that it was unsuitable for LIBs

as it was electrochemically reduced at the negative electrode, thus leading to capacity fade<sup>76–78</sup>. It was later shown that longer alkyl chains or substituting the alkyl chains with aryl groups increase the electrochemical stability and improve the flame retarding abilities of phosphate based flame retardants<sup>78–80</sup>.

Triphenyl phosphate (TPP) is one such example, where the methyl groups of TMP have been substituted to phenyl groups<sup>80,81</sup>. TPP has been found to have two flame retarding effects: firstly by scavenging radicals in the flame, thus preventing flame propagation, and secondly by forming a layer of char, suffocating the flame<sup>76,82,83</sup>. TPP affects the cycle performance and life in minor ways<sup>83–85</sup>, but high TPP contents have been shown to increase impedance of both negative and positive electrodes<sup>86,87</sup>.

## 1.5 Aim of this thesis

The aim of this thesis is mainly to increase the understanding and highlight the importance of the electrolyte and of temperature effects in lithium-ion batteries. Furthermore the importance of accurate materials characterizations in general, and of electrolyte mass transport characterizations specifically, is highlighted. The thesis will give a few examples of characterizations of electrolyte systems with very different mass transport properties, and show how the different electrolytes the performance of a commercial large-format battery in a PHEV application. Additionally, a way of benchmarking electrolytes including all limitations in mass transport is explored and illustrated for several different systems.

## Chapter 2: Methods

All electrochemical experiments, electrolyte preparations, and cell assemblies were performed in a glovebox filled with dry argon, except for those related to Paper V, which were performed in an Espec BPU-3 temperature chamber. Additionally for Paper II, the electrochemical experiments were performed in a custom-built thermo-electric Peltier oven located in the glovebox. Modeling was done using COMSOL Multiphysics, and optimization using Matlab.

### 2.1 Materials

Liquid electrolytes were prepared by dissolving a salt: either lithium (Li) hexafluorophosphate ( $\text{PF}_6^-$ ) or Li bis(trifluoro-methanesulfonyl)imide (TFSI $^-$ ), in a solvent: either ethylene carbonate (EC) and diethyl carbonate (DEC) in a 1:1 ratio by weight, 1-ethyl-3-methylimidazolium (Emim) TFSI and EC in a 2:1 ratio by weight, or acetonitrile (ACN). For Paper I, triphenyl phosphate (TPP) was added to preprepared electrolyte with 1 M  $\text{LiPF}_6$  in a 1:1 mixture by weight of EC:DEC. For Papers II and III, the solvent concentration was recorded during electrolyte preparation, to obtain the molar volumes.

Solid polymer electrolytes were prepared using the solvent casting method by dissolving Li Triflate (Tf $^-$ ) and poly(ethyleneoxide) (PEO) in ACN and then dried in the glovebox for 24 hours, to evaporate the ACN.

Gelled polymer electrolytes were also prepared with the solvent casting method by dissolving  $\text{LiPF}_6$ , poly(vinylidenefluoride-co-hexafluoropropylene) (PVdF-co-HFP), and a 6:4 mixture by weight of EC and propylene carbonate (PC) in dimethyl carbonate (DMC) and then dried in the glovebox for 30 hours to evaporate the DMC.

Full cells for Paper I were assembled using graphite negative, and lithium iron phosphate positive electrodes.

The large-format commercial cell in Paper V contained a graphite negative, and a lithium nickel manganese cobalt oxide (NMC) positive

electrode, and an electrolyte consisting of LiPF<sub>6</sub>, EC, ethyl methyl carbonate (EMC), and DMC. Additionally, the electrolyte contained a number of unknown additives.

## 2.2 Experimental

All electrochemical testing was performed using a Gamry PCI4/750 potentiostat, except the full-cell testing in Paper I where a Bio-Logic VMP2 potentiostat was used, and for Paper V where a PEC SBT0550 cell tester was used.

Density and viscosity measurements were conducted simultaneously with an Anton Paar DMA 4500M/Lovis 2000M using an oscillating U-tube for the density and the falling sphere method for the viscosity. Data was collected at 10, 25 and 40 °C in two consecutive temperature scans, up and down, to verify that the scan direction did not affect the results.

Flash points were measured using a Petrotest ABA 4 equipment with tests performed according to the Abel method. Self-extinguishing times were measured by placing ~0.5 g on a watch glass and exposing it to a burner for 3 s to allow ignition. The time required for the flame to self-extinguish was recorded and normalized against the electrolyte mass.

Ionic conductivity measurements were performed using a Consort K912 conductometer with a SK41T four-electrode probe, pre-calibrated outside the glovebox using KCl standard solutions, for the liquid electrolytes or using electrochemical impedance spectroscopy (EIS) for the solid electrolytes (the solid polymer and the gelled polymer electrolytes). When using EIS, the ionic conductivity was extracted from the high frequency intercept of the x-axis in a Nyquist plot (Figure 2) using Equation 1.

$$\kappa = \frac{L}{A \cdot R_{\text{electrolyte}}} \quad (1)$$

where  $\kappa$  is the ionic conductivity,  $L$  the thickness of the electrolyte,  $A$  the area of the electrolyte, and  $R_{\text{electrolyte}}$  the electrolyte resistance.

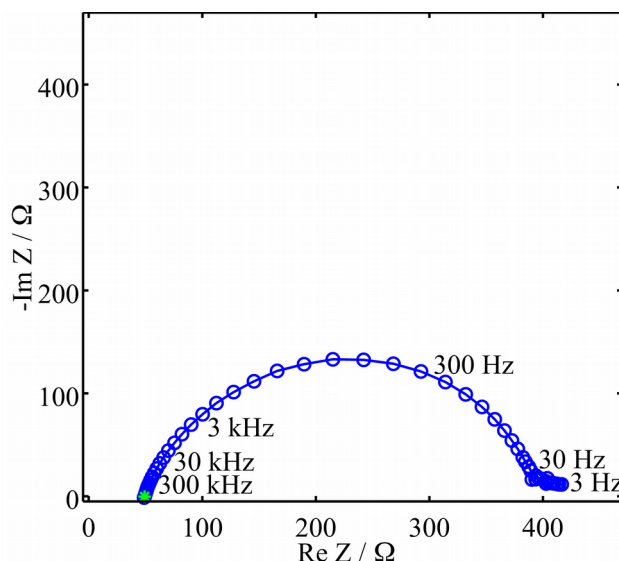


**Figure 2:** Typical Nyquist plot from an EIS measurement, with the electrolyte resistance marked by the asterisk.

Concentration cells were assembled by placing a glass microfibre filter (approximately  $5 \times 50$  mm) on a microscope slide and soaking its ends with enough electrolyte of two different concentrations to ensure electrolytic contact between the two electrolyte concentrations at midpoint. The open-circuit potential (OCP) was then measured for 10 minutes, to enable the potential to stabilize, using two Li-foil strips as electrodes.

Galvanostatic polarization experiments were conducted in symmetrical Li cylindrical cells. Two Li-foil discs were used as electrodes with stainless steel current collectors, and a Whatmann GF/A filter was used as a separator, to minimize convection and leakage. The separator was fitted inside a teflon cylinder. In order to make sure that the characterization did not depend on the cell geometry, two different separator diameters (6 and 12 mm) and thicknesses (500 and 1000  $\mu\text{m}$ ) were used. After assembly, the cells were polarized using different current densities and polarization times and the OCP relaxation profiles were measured

afterwards. For the full characterizations, Papers II and III, the entire OCP relaxation profiles were used, while for Papers I and IV, only the initial value of the OCP was used (Figure 3). The current densities were chosen so that the relaxation potential directly after current shut-off was between 5 and 50 mV, except in Paper IV where the initial relaxation potentials were kept between 5 and 30 mV, to minimize noise while avoiding dendrite formation.

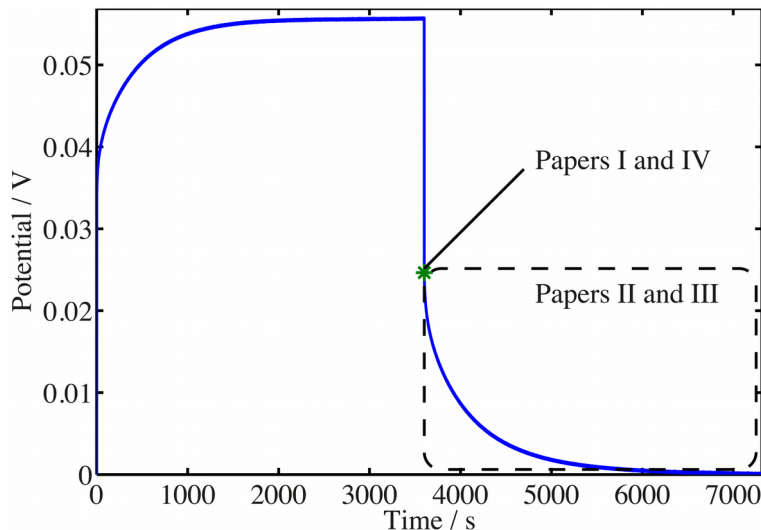


**Figure 3:** Typical galvanostatic polarization experiment, with the type of extracted information for the Papers I-IV marked.

Cyclic voltammetry was performed using stainless steel/Li-foil cells between 0 and 5 V vs Li/Li<sup>+</sup> to investigate the electrochemical stability using a scan-rate of 1 mV s<sup>-1</sup>.

The full-cells in Paper I were galvanostatically cycled at C/10 (0.88 A m<sup>-2</sup>), and subsequently subjected to the EUCAR (Figure 4) hybrid pulse power characterization (HPPC) test at 60 % SOC <sup>88</sup>. The cycle is charge-neutral. The cell was not temperature controlled in any way.

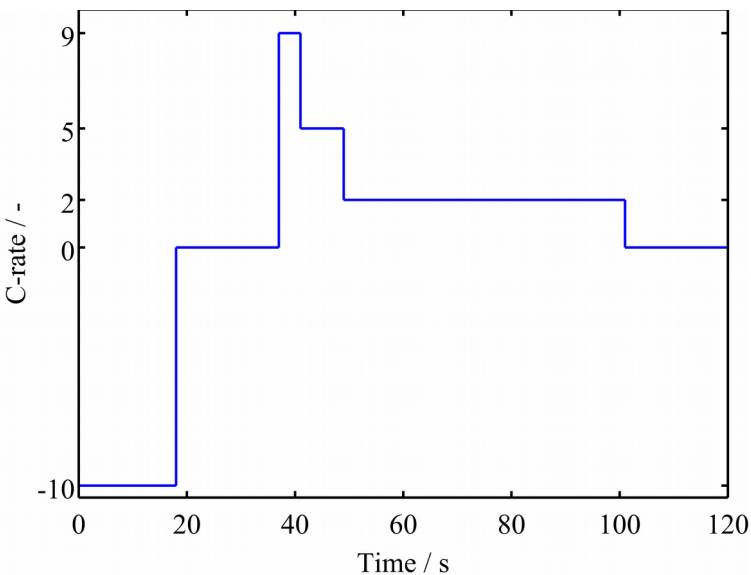


**Figure 4:** EUCAR hybrid pulse power characterization test used in Paper I<sup>88</sup>. Positive currents correspond to charging.

The cell used in Paper V, was subjected to slightly modified versions of the ISO Dynamic Discharge Power Profile (ISO DDPP) A and B (Figure 5) at 75.5 % SOC<sup>89</sup>, converted from power basis to current basis with  $P_{max}$  corresponding to the maximum rated current of 8C (200 A). ISO DDPP are charge-depleting cycles, with a total SOC difference of -34.2 % between the start and end point for the two combined cycles. The cell was mounted on a heat sink that was temperature controlled using a Lauda XT550 process thermostat and covered in several layers of plastic foam, to create near-adiabatic conditions at all boundaries except the surface connected to the heat sink. Six type K thermocouples were connected to the cell, as seen in Figure 6. All thermocouples were electrically insulated using a thin plastic film to avoid interference from the aluminum cell case, and then attached to the cell using copper tape with a high thermal conductivity.

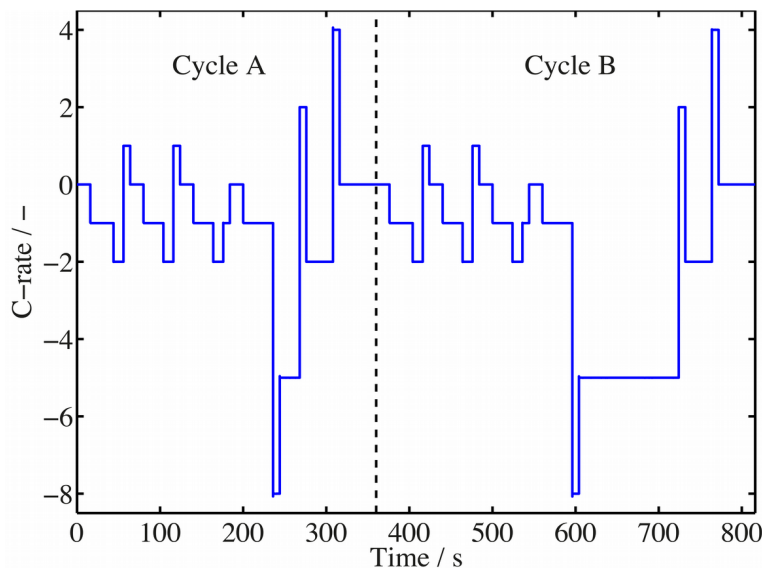


**Figure 5:** Slightly altered ISO DDPP A and B converted to current basis, used in Paper V<sup>89</sup>. Positive currents correspond to charging.

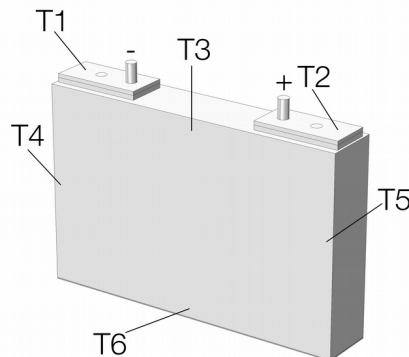


**Figure 6:** Placement of the temperature probes on cell used in Paper V.

## 2.3 Modeling

### 2.3.1 Electrolyte model

For Papers II and III, a one-dimensional mass transport model for a binary electrolyte in one solvent (i.e. the EC:DEC mixture in Paper II is assumed to behave as one species) based on the Maxwell-Stefan equation developed by Nyman *et al.* was set up<sup>90</sup>. Electrolyte mass transport resistivity, used in Papers I-IV, has a theoretical foundation in the same model. The governing equation, boundary conditions, and initial conditions to describe the concentration profiles are found below in Equations 2-5:

$$\varepsilon_L \frac{\partial c_{\text{salt}}}{\partial t} = - \frac{\partial}{\partial x} N_+ \quad (2)$$

$$N_+ = - \left( 1 - c_{\text{salt}} V_m^{\text{salt}} \right) \left( \left( 1 + \frac{\partial \ln f_\pm}{\partial \ln c_{\text{salt}}} \right) \frac{c_{\text{tot}}}{c_{\text{solv}}} \varepsilon_L^\beta \tilde{D}_{\text{salt}} \frac{\partial c_{\text{salt}}}{\partial x} + \frac{(1 - t_+^{\text{solv}})}{F} i \right) \quad (3)$$

Boundary and initial conditions:

$$N_+ = 0 \quad \text{at } x = 0 \text{ and } x = L \quad (4)$$

$$c_{\text{salt}} = c_{\text{salt}}^0 \quad \text{at } t = 0 \quad (5)$$

where  $\varepsilon_L$  is the electrolyte volume fraction (i.e. porosity),  $c$  the concentration,  $t$  the time,  $N_+$  the anion flux,  $V_m$  the partial molar volume,  $1 + \partial \ln f_\pm / \partial \ln c_{\text{salt}}$  the thermodynamic enhancement factor for the salt,  $\beta$  the Bruggeman coefficient,  $\tilde{D}_{\text{salt}}$  the salt diffusion coefficient with respect to the thermodynamic driving force,  $t_+^{\text{solv}}$  the Li-ion transport number with respect to the solvent,  $F$  the Faraday constant ( $96485 \text{ C mol}^{-1}$ ),  $i$  the current density, and  $L$  the cell length. Additionally, an expression for the potential difference between two Li-metal reference electrodes is required:

$$\Delta \Phi_L = \int_0^L \frac{\partial \Phi_L}{\partial x} dx = \int_0^L \left( -\frac{i}{\varepsilon_L^\beta \kappa} + \frac{2RT}{Fc_{\text{salt}}} \left( 1 + \frac{\partial \ln f_\pm}{\partial \ln c_{\text{salt}}} \right) \left( 1 - t_+^{\text{solv}} \right) \frac{\partial c_{\text{salt}}}{\partial x} \right) dx \quad (6)$$

where  $\Phi_L$  is the electrolyte potential,  $\kappa$  the conductivity,  $R$  the ideal gas constant ( $8.314 \text{ J K}^{-1}\text{mol}^{-1}$ ), and  $T$  the temperature. In a concentration cell, where no net current is passing through the electrolyte, the expression simplifies to:

$$\frac{\partial \Phi_L}{\partial \ln c_{\text{salt}}}|_{i=0} = \frac{2RT}{F} \left( 1 + \frac{\partial \ln f_{\pm}}{\partial \ln c_{\text{salt}}} \right) \left( 1 - t_+^{\text{solv}} \right) \quad (7)$$

From the transport properties used above, two apparent transport properties, which are more commonly cited, can be defined. They have the disadvantage that they are less general, since they depend on the solvent flux factor,  $(1 - c_{\text{salt}} V_m^{\text{salt}})$ , and therefore which ion that participates in the electrode reaction. These two properties are the apparent diffusion coefficient,  $D_{\text{App}}$ , and the transport number with respect to the room,  $t_+$ :

$$D_{\text{App}} = \tilde{D}_{\text{salt}} \left( 1 + \frac{\partial \ln f_{\pm}}{\partial \ln c_{\text{salt}}} \right) \frac{c_{\text{tot}}}{c_{\text{solv}}} \left( 1 - c_{\text{salt}} V_m^{\text{salt}} \right) \quad (8)$$

$$t_+ = 1 - (1 - t_+^{\text{solv}}) \left( 1 - c_{\text{salt}} V_m^{\text{salt}} \right) \quad (9)$$

The electrolyte mass transport resistivity, a benchmarking method and parameter used in Papers I-IV, can be defined using the same model as mentioned earlier, here for a binary electrolyte in one solvent:

$$\frac{-(\partial \Phi_L / \partial x)_{S.S.}}{i} = \frac{1}{\kappa} + \frac{2RT}{F^2 c_{\text{salt}}} \frac{c_{\text{solv}}}{c_{\text{tot}}} \frac{(1 - t_+^{\text{solv}})^2}{\tilde{D}_{\text{salt}}} \quad (10)$$

where  $c_{\text{tot}}$  is the total concentration in the electrolyte, i.e.  $2c_{\text{salt}} + c_{\text{solv}}$ .

Several of the parameters/coefficients for LiPF<sub>6</sub> in EC:DEC, as well as many of the properties for Paper V, are found to depend on temperature. That temperature dependency is implemented through an Arrhenius expression:

$$n(T) = n(T_{\text{ref}}) \cdot e^{\left( \frac{E_a}{R} \right) \left( \frac{1}{T_{\text{ref}}} - \frac{1}{T} \right)} \quad (11)$$

where  $T_{ref}$  is a reference temperature at which the property  $n$  is known, and  $E_a$  the activation energy for the temperature dependence.

### 2.3.2 Full cell model

The electrochemical model for the full cell in Paper V was set up using the physics interface “Lithium-Ion Battery” in COMSOL Multiphysics. The model is based on the work of Doyle, Fuller, and Newman<sup>91–93</sup>. A 2D geometry is used corresponding to a slice across the jellyroll with the thickness of one cell layer (current collector | electrode | separator | electrode | current collector), see Figure 7, also including a color map of the materials in the model.

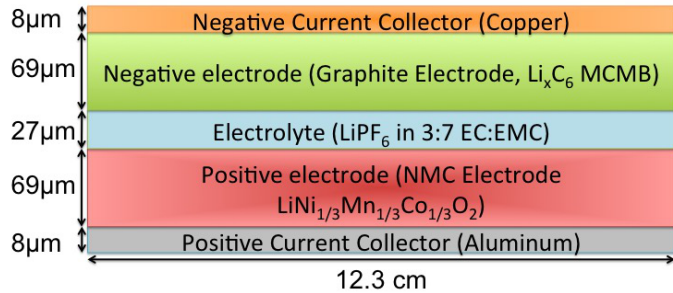


**Figure 7:** 2D Geometry and material color map used in the electrochemical model in Paper V. Only half of the current collector thicknesses are included in the model as they are coated on both sides.

The domain equations in the electrolyte are the conservation of current (Equation 12), and a mass balance in the electrolyte (Equation 13):

$$i_{tot} = \epsilon_L^\beta \nabla \cdot \left( -\kappa \nabla \Phi_L + \frac{2\kappa RT}{F} \left( 1 + \frac{\partial \ln f_\pm}{\partial \ln c_{salt}} \right) \left( 1 - t_+^{solv} \right) \nabla \ln c_{salt} \right) \quad (12)$$

$$\epsilon_L \frac{\partial c_{salt}}{\partial t} + \epsilon_L^\beta \nabla \cdot (-D_{App} \nabla c_{salt}) = \frac{-i_{tot}}{F} t_+ \quad (13)$$

For the porous electrodes, the domain equations are conservation of current, porous electrode current density, total current from charge

transfer reactions, and a mass balance within the electrode particles, using the Butler-Volmer equation for the charge-transfer kinetics:

$$\nabla \mathbf{i}_s = -i_{tot} \quad (14)$$

$$\mathbf{i}_s = -\sigma_s \nabla \Phi_s \quad (15)$$

$$i_{tot} = \hat{A} i_{loc} \quad (16)$$

$$\frac{\partial c_s}{\partial t} = \nabla \cdot (-D_s \nabla c_s) \quad (17)$$

$$i_{loc} = i_{0,i} \left( \exp\left(\frac{\alpha_{a,i} F \eta}{RT}\right) - \exp\left(\frac{-\alpha_{c,i} F \eta}{RT}\right) \right) \quad (18)$$

where  $\mathbf{i}_s$  is the current density in the electrode phase,  $\Phi_s$  the electrode potential,  $i_{tot}$  ( $\text{A m}^{-3}$ ) the electrochemical reaction current source,  $\sigma_s$  the electronic conductivity,  $\hat{A}$  the specific area of the electrode particles,  $c_s$  the lithium-ion concentration in the electrode particles,  $i_0$  the exchange current density,  $\alpha$  the electrochemical reaction symmetry factor, and  $\eta$  the overpotential defined as:

$$\eta = \Phi_s - \Phi_L - E_{Eq} \quad (19)$$

where  $E_{eq}$  is the electrode equilibrium potential.

Furthermore, several properties change with the SOC, defined as:

$$SOC = \frac{c_s}{c_{s,max}} \quad (20)$$

### 2.3.3 Thermal model

The thermal model in Paper V was set up using the physics interface “Heat Transfer in Solids” in COMSOL Multiphysics. A detailed 3D geometry of the commercial battery was used (Figures 8 and 9, also including a color map of the materials in the model). The void spaces inside the battery are assumed to be filled with argon gas.

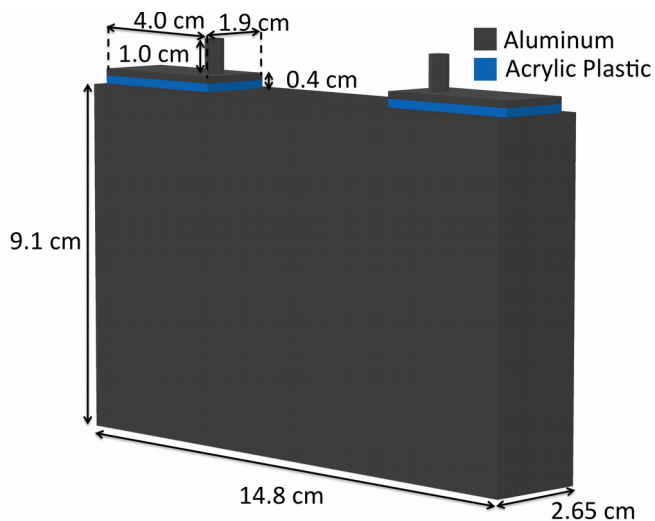


**Figure 8:** 3D Geometry and material color map of the battery exterior used in the thermal model in Paper V.

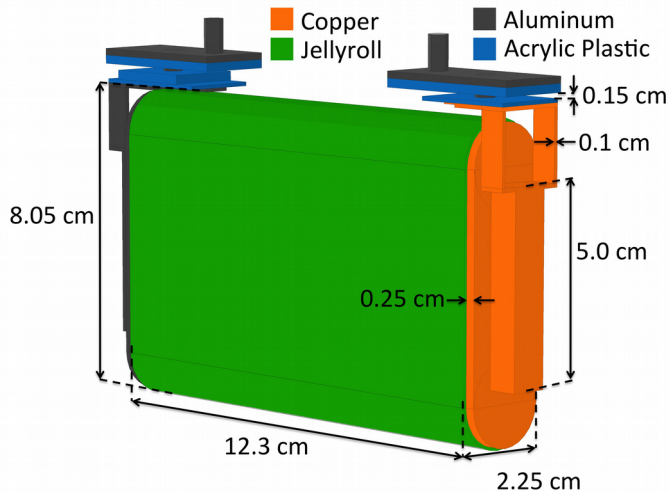


**Figure 9:** 3D Geometry and material color map of the battery interior used in the thermal model in Paper V.

The domain equation for the entire geometry is a thermal energy balance, neglecting all modes of heat transfer except conduction <sup>32</sup>:

$$\rho C_p \frac{\partial T}{\partial t} = \nabla \cdot (k \nabla T) + Q \quad (21)$$

where  $\rho$  is the density,  $C_p$  the heat capacity at constant pressure,  $k$  the thermal conductivity, and  $Q$  the heat generation rate. Heat is generated in the jellyroll, according to Equation 22, and in the current collectors/terminals by joule heating according to Equation 23. The heat generated in the jellyroll is calculated from the electrochemical model in and is averaged for the volume of the jellyroll, and in the current collectors/terminals using the physics interface “Electric Currents” locally in the 3D geometry.

$$Q_{Jellyroll} = \frac{\int_{Battery} \left( i_{tot} \eta + i_{tot} \left( T \frac{\partial E_{Eq}}{\partial T} \right) - (\mathbf{i}_s \cdot \nabla \Phi_s + \mathbf{i}_L \cdot \nabla \Phi_L) \right) d\Omega}{\int_{Battery} d\Omega} \quad (22)$$

$$Q_{Joule} = \mathbf{i}_s \cdot \nabla \Phi_s \quad (23)$$

where  $d\Omega$  is a volume element in the battery. The first term on the right hand side in Equation 22 is the irreversible heat generation, and the second term the reversible heat generation (entropic heat). The simulated potential is calculated as the combination of the potential from the electrochemical model and the overpotentials of the current collectors/terminals.

## 2.4 Optimization

The optimization of all parameters in Paper II, the temperature dependent fits in this thesis, and the diffusion coefficient and transport number in Paper III, were done using the script “lsqnonlin” in Matlab which uses the Levenberg-Marquardt algorithm. The other parameters were optimized using the least squares method.

The cationic transport number and the diffusion coefficient were obtained by fitting the model described in section 2.3 to experimental data of

relaxation profiles from galvanostatic polarization experiments. The thermodynamic enhancement factor, which is coupled to the transport number, is simultaneously obtained from the concentration cell results, which are fed to the optimization. OCP relaxation data points were evenly distributed over dimensionless time (Equation 24), and polarization currents and times were chosen to ensure finite conditions, avoiding dendrite formation, and minimizing the noise.

$$\tau = \frac{\sqrt{t_{\text{polarization}}}}{\sqrt{t} + \sqrt{t - t_{\text{polarization}}}} \quad (24)$$



## Chapter 3: Results and discussion

This section summarizes the main results of the Papers included in this thesis. The results are divided into three sections: one dealing with electrolyte characterizations (Papers I-IV), one dealing with the effect of the flame retardant TPP in a HEV application (Paper I), and finally a section on the thermal modeling of a commercial large-format lithium-ion battery (Paper V).

### 3.1 Electrolyte characterizations

The Onsager reciprocal relationship states that to fully describe the mass transport phenomena in an electrolyte with  $n$  components,  $n(n-1)/2$  transport properties are needed<sup>30,90,94–96</sup>, i.e. three transport properties for a binary electrolyte in one solvent. The fact that the number of needed transport properties scales with the number of components in the electrolyte is why solvent mixtures are treated as one species. The three transport properties are the ionic conductivity, diffusion coefficient, and the transport number. Additionally, a thermodynamic property related to the activity coefficient is needed: the thermodynamic enhancement factor. Because of the complexity and tediousness of the available methods, full characterizations are scarce. Full characterizations based on electrochemical methods have been made for solid polymer electrolytes<sup>97–100</sup>, gelled polymer electrolytes<sup>101,102</sup>, and organic carbonate electrolytes<sup>30,90,103</sup>. In addition, physical methods such as Raman spectroscopy, UV/Vis spectroscopy, and nuclear magnetic resonance spectroscopy, have been used for full characterizations<sup>104–107</sup>.

#### 3.1.1 Density, viscosity, and partial molar volumes

Although not explicitly included in most battery electrolyte models, the physical properties density and viscosity affect the performance to a large degree. The partial molar volumes are included in the electrolyte mass transport model described in Section 2.3.1. They can be seen as the volume of one mole of that species in that specific environment.

## 24 | Chapter 3: Results and discussion

Determining partial molar volumes is done by volume or density fraction functions, as seen in Equations 25 and 26:

$$c_{salt} V_m^{salt} + c_{solv} V_m^{solv} = 1 \quad (25)$$

$$\frac{M_{w,salt}}{V_m^{salt}} y_{salt} + \frac{M_{w,solv}}{V_m^{solv}} y_{solv} = \rho \quad (26)$$

where  $\rho$  is the electrolyte density,  $M_w$  is the molecular weight, and  $y_{salt}$  the mass-fraction of the salt. By recording the solvent mass / concentration during electrolyte preparation, the molar volumes can be extracted by linear fitting of  $c_{salt}$  vs  $c_{solv}$  or  $y_{salt}$  vs  $\rho$ , where the slope is related to the salt's partial molar volume, and the intercept to the solvent's. The advantage of using density compared to concentration when determining the partial molar volumes is that it is difficult to prepare electrolytes at different, constant, temperatures, especially since some solvents, e.g. EC:DEC, are semi-crystalline at lower temperatures, and electrolytes are stabilized through the salt, thus making electrolyte preparation impossible. The disadvantage is that it requires one more experiment, and therefore an additional source of error.

Figure 10 shows the densities of LiPF<sub>6</sub> in EC:DEC and LiTFSI in ACN as functions of concentration at 10 °C, 25 °C, and 40 °C. A linear relationship is observed, indicating constant partial molar volumes. The partial molar volumes, calculated using both density and concentration, are summarized in Table 2. It can be seen that the two methods coincide fairly well, but not perfectly.

**Table 2:** Partial molar volumes for LiPF<sub>6</sub>, LiTFSI, EC:DEC, and ACN calculated using both concentration (Conc.) and density (Dens.) data at 10 °C, 25 °C, and 40 °C.

$V_m \cdot 10^6 / \text{m}^3 \text{ mol}^{-1}$	10 °C, Dens.	25 °C, Dens.	25 °C, Conc.	40 °C, Dens.
LiPF <sub>6</sub>	57.0	56.8	60.8	56.5
LiTFSI	148.1	148.2	141.9	143.5
EC:DEC	89.5	90.7	91.6	92.1
ACN	49.1	49.9	54.1	50.7

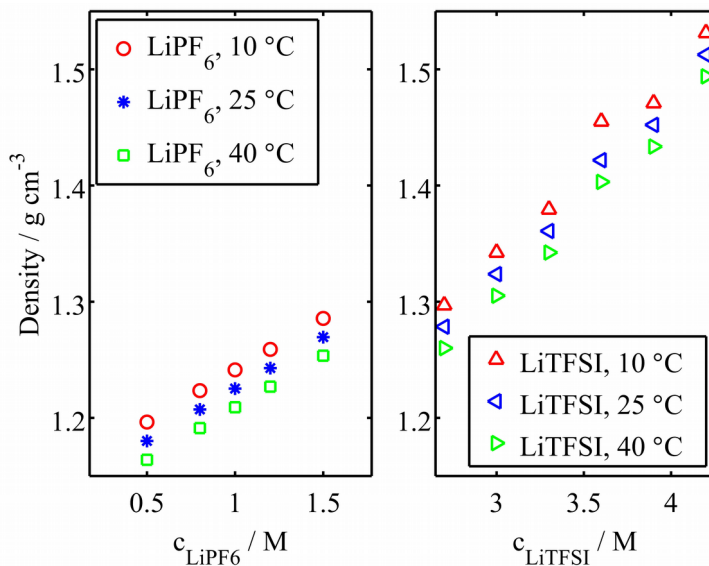


**Figure 10:** Density for LiPF<sub>6</sub> in EC:DEC and LiTFSI in ACN as functions of concentration at 10 °C, 25 °C, and 40 °C.

Viscosity highly affects both the ionic conductivity and the salt diffusion coefficient of the electrolyte, and observed trends for these two parameters are often just effects of viscosity. This effect can be probed by taking the product of the transport property and the viscosity, where a

constant product indicates that the effect is due to viscosity. Figure 11 illustrates this effect for the electrolyte used in Paper I, LiPF<sub>6</sub> in EC:DEC with the additive TPP, in terms of the Walden product:

$$W = \Lambda \mu \quad (27)$$

where  $W$  is the Walden product,  $\Lambda$  the limiting molar conductivity ( $\Lambda = \kappa / c_{\text{salt}}$ ), and  $\mu$  the viscosity. The Walden product in Figure 11 is fairly constant, and the observed change in ionic conductivity can be concluded to be mainly due to viscosity changes.

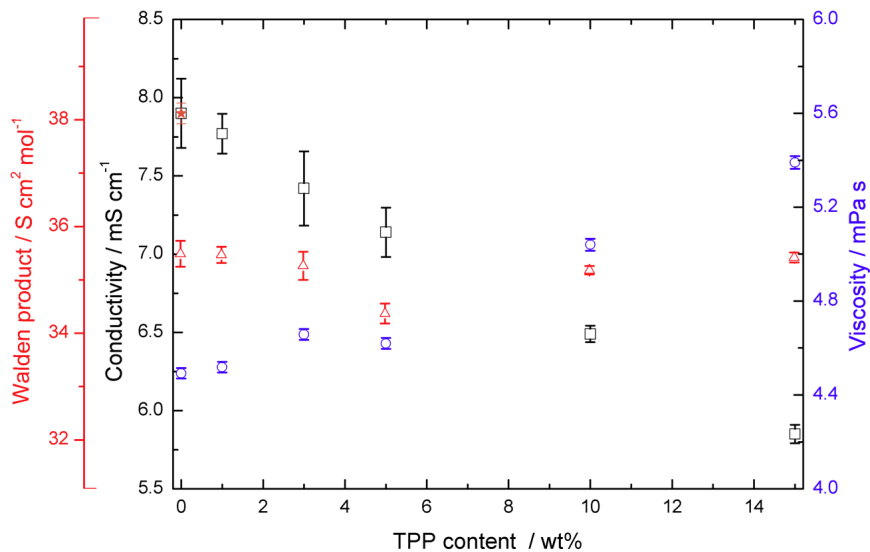


**Figure 11:** Ionic conductivity (□), viscosity (○), and the Walden product (Δ, Equation 27) for LiPF<sub>6</sub> and TPP in EC:DEC.

The viscosities for LiPF<sub>6</sub> in EC:DEC and LiTFSI in ACN are displayed in Figure 12 as functions of concentration at 10 °C, 25 °C, and 40 °C. At the extremely high LiTFSI concentrations used in Paper III, the viscosity changes rapidly with concentration, leading to a large change in the transport properties for small concentration changes.

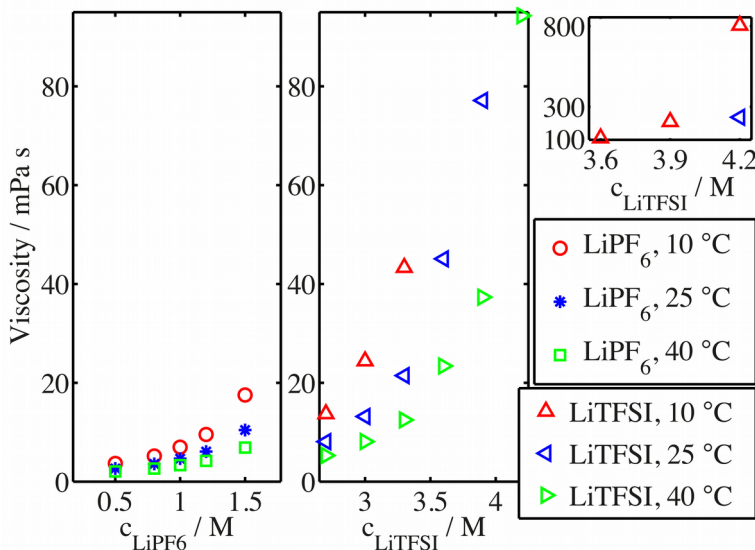


**Figure 12:** Viscosity for  $\text{LiPF}_6$  in EC:DEC and LiTFSI in ACN as functions of concentration at 10 °C, 25 °C, and 40 °C. Top right figure shows the viscosities for the LiTFSI samples outside the scale of the main plot.

### 3.1.2 Ionic conductivity

The ionic conductivity is the ohmic component of the electrolyte performance, and is a measure of the system's ability to transport charge (i.e. ions). It is readily measured using either a conductometer, or EIS, and the relative simplicity has made it the most commonly studied electrolyte performance parameter. Figure 13 shows the ionic conductivity for  $\text{LiPF}_6$  in EC:DEC, LiTFSI in EmimTFSI:EC, LiTFSI in ACN,  $\text{LiPF}_6$  in PVdF-co-HFP and EC:PC, and  $\text{LiPF}_6$  and TPP in EC:DEC, in the relevant salt/additive content range for the respective system at 25 °C. Since the content ranges are very different, and correspond to different species, inter-system comparisons regarding concentration is difficult. However, trends can be seen. The liquid, not superconcentrated (<3.6 M) systems show similar conductivities around 5-15 mS cm<sup>-1</sup>, while the gelled polymer and the superconcentrated electrolyte has conductivities around ~ 1 mS cm<sup>-1</sup>.

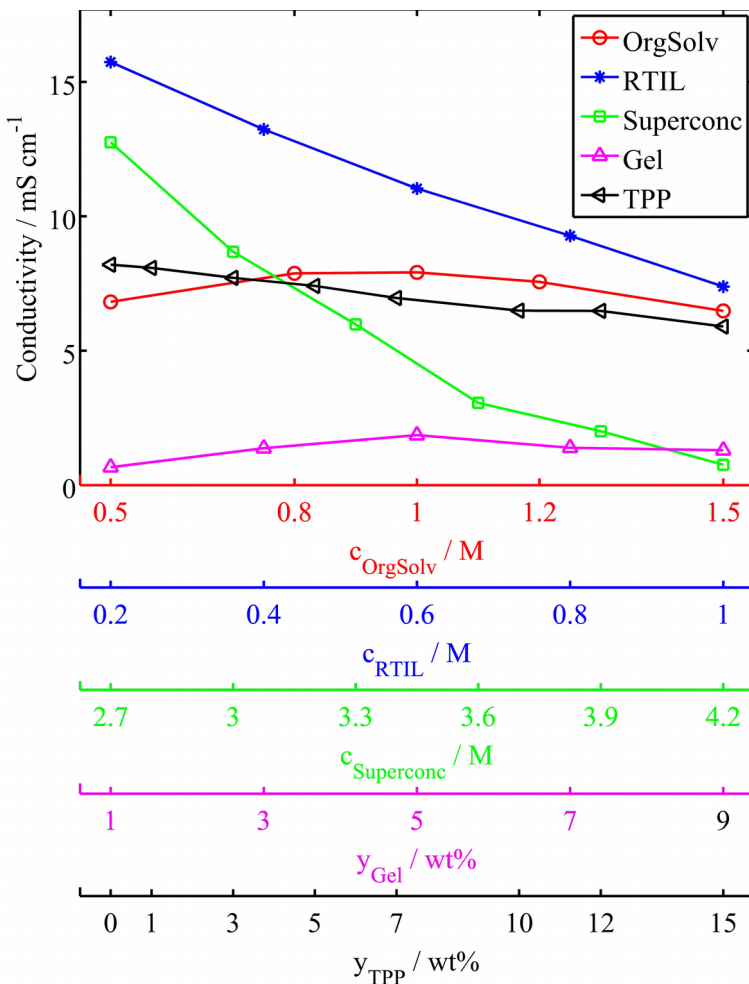


**Figure 13:** Ionic conductivities for LiPF<sub>6</sub> in EC:DEC, LiTFSI in EmimTFSI:EC, LiTFSI in ACN, LiPF<sub>6</sub> in PVdF-co-HFP:EC:PC, and LiPF<sub>6</sub> and TPP in EC:DEC, as functions of salt/additive content in that system's relevant concentration range at 25 °C.

Generally, the ionic conductivity increases with salt concentration since the number of ions, and therefore charge carriers, increases. However, if the concentration is too high, both ion pairing occurs and the viscosity

increases (Section 3.1.1), resulting in a conductivity decrease<sup>108</sup>. Analyzing the behavior of the different systems, this effect is clear for the organic-solvent system and the gelled polymer. The RTIL and the superconcentrated systems already contain a large number of ions, and adding more salt (i.e. ions) to those systems does not affect the ion concentration to a large degree but the viscosity a lot, thus lowering the ionic conductivity. When adding TPP to the electrolyte, the salt concentration decreases and the viscosity increases, both leading to lowered conductivity. Clearly, optimizing conductivity for a complex electrolyte with several solvents and additives is not trivial.

The ionic conductivity is a strong function of temperature. Figure 14 shows the ionic conductivity as a function of concentration at 10 °C, 25 °C, and 40 °C as well as a polynomial fit (Equation 28). The polynomial is slightly different than the temperature dependent fit given in Paper II, as only the ionic conductivity itself is temperature dependent, and not the individual coefficients, but still assuming Arrhenius temperature dependence (Equation 11). The fit not as good as in Paper II, but simpler to implement in a model.

$$\kappa(c, T) = e^{\left(\frac{15840}{R}\right)\left(\frac{1}{298} - \frac{1}{T}\right)} \left(1.147 c_{\text{LiPF}_6}^3 - 22.38 c_{\text{LiPF}_6}^{1.5} + 29.15 c_{\text{LiPF}_6}\right) \quad (28)$$

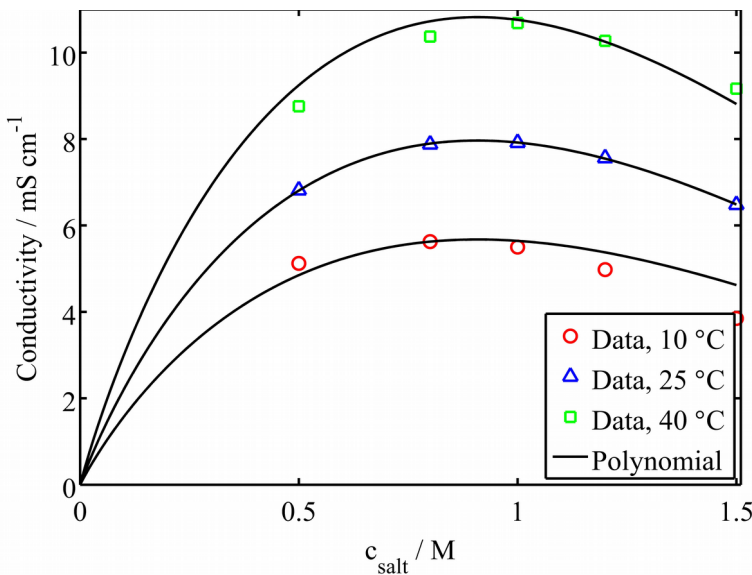


**Figure 14:** Experimental (markers) and polynomial fit (solid lines, Equation 28) of ionic conductivity for  $\text{LiPF}_6$  in EC:DEC as a function of concentration at 10 °C, 25 °C, and 40 °C.

### 3.1.3 Diffusion coefficient, transport number, and thermodynamic enhancement factor

When passing a current through an electrolyte with a non-unity transport number, concentration gradients are built up due to limitations in ion transport. These concentration gradients lead to polarization, i.e. potential losses. The material properties used to describe this phenomenon for a binary electrolyte using concentrated electrolyte theory are the diffusion coefficient, the transport number, and the thermodynamic enhancement factor.

The diffusion coefficient can be defined in two different ways: either based on the thermodynamic driving force, or based on salt concentration gradients. The latter definition, termed apparent diffusion coefficient, is the most commonly cited. Figure 15 shows the diffusion coefficients for  $\text{LiPF}_6$  in EC:DEC and  $\text{LiTFSI}$  in ACN at 25 °C.

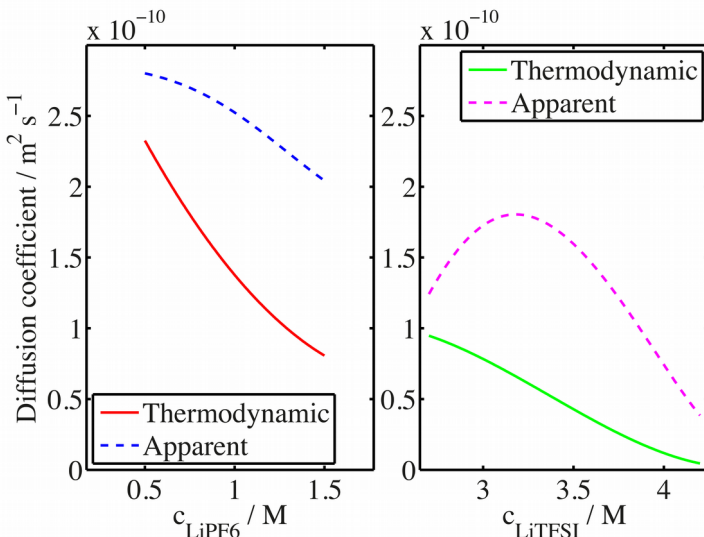


**Figure 15:** Diffusion coefficients based on the thermodynamic driving force (solid lines) and the apparent diffusion coefficients (dashed lines) for LiPF<sub>6</sub> in EC:DEC and LiTFSI in ACN at 25 °C.

The transport number is a measure of the fraction of current being carried by a specific ion, e.g. the lithium ion in the case of lithium-ion batteries. Like the diffusion coefficient, the transport number can also be defined in two ways: with respect to the solvent, or to the room, with the latter being the most commonly cited. Figure 16 shows the transport numbers for LiPF<sub>6</sub> in EC:DEC and LiTFSI in ACN at 25 °C. The difference in the transport numbers for the two systems is immense, and the advantage of using supercontrated electrolytes is obvious: more current is carried by the wanted species, the lithium-ion, thus generating smaller concentration gradients. For LiPF<sub>6</sub> in EC:DEC the transport numbers decrease with concentration, meaning that the lithium-ion-solvent interactions increase compared to anion-solvent interactions. For LiTFSI in ACN the situation is reversed, with the anion-solvent interactions growing steadily stronger.

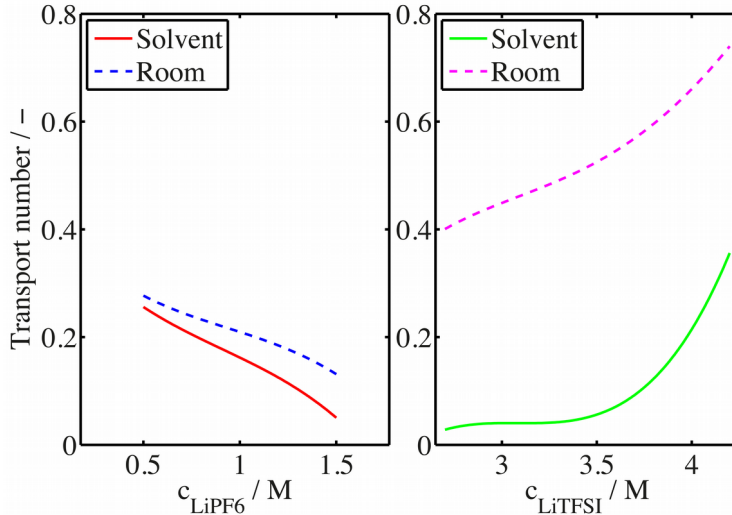


**Figure 16:** Transport numbers with respect to the solvent (solid lines) and to the room (dashed lines) for LiPF<sub>6</sub> in EC:DEC and LiTFSI in ACN at 25 °C.

The thermodynamic enhancement factor is a measure of how the thermodynamic driving force relates to concentration gradients, and depends on the activity coefficient. At infinite dilution, this factor is unity and the electrolyte behaves like an ideal electrolyte. Figure 17 shows the thermodynamic enhancement factor for LiPF<sub>6</sub> in EC:DEC and LiTFSI in ACN at 25 °C. Not surprisingly, the superconcentrated electrolyte is highly non-ideal at higher concentrations, and the thermodynamic driving force will be larger for a given concentration difference.

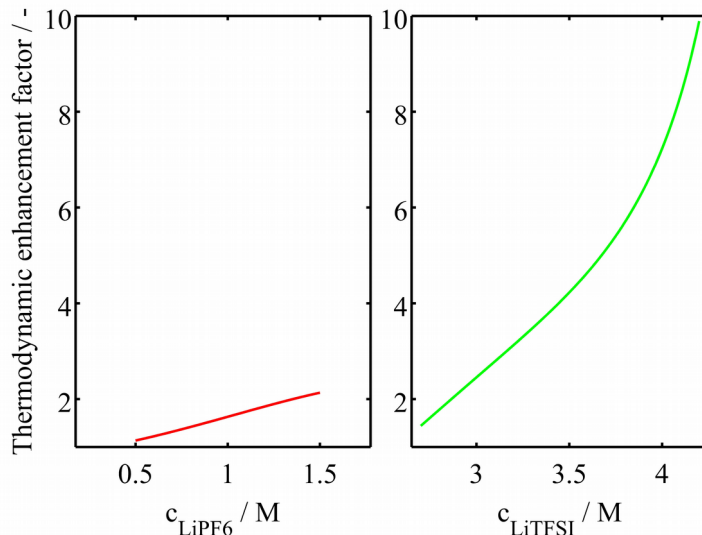


**Figure 17:** Thermodynamic enhancement factors for  $\text{LiPF}_6$  in EC:DEC and  $\text{LiTFSI}$  in ACN at 25 °C.

In Paper II, no temperature dependent fit for the diffusion coefficient, transport number, and the thermodynamic enhancement factor was included because of the very different behavior of the electrolyte at the studied temperatures, especially at 10 °C. However, this fitting has been included in this thesis. Table 3 shows the Arrhenius activation energies (Equation 11) for these three properties based on the polynomials at 25 °C. The resulting fit can be seen in Figure 18.

**Table 3:** Arrhenius activation energies (Equation 11) of the diffusion coefficient, transport number, and thermodynamic enhancement factor for  $\text{LiPF}_6$  in EC:DEC, with  $T_{\text{ref}} = 25$  °C.

	$\tilde{D}_{\text{LiPF}_6}$	$t_+^{\text{EC:DEC}}$	$(1 + \partial \ln f_\pm / \partial \ln c_{\text{LiPF}_6})$
$E_a / \text{J mol}^{-1}$	12360	9890	8260

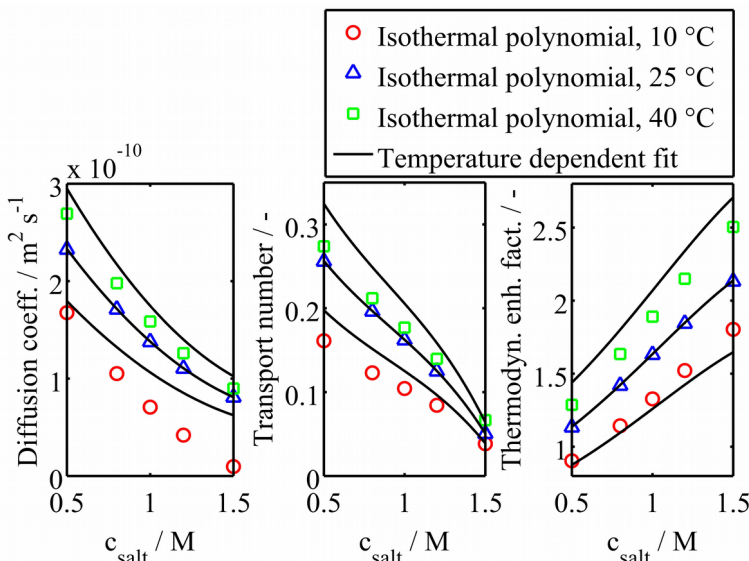


**Figure 18:** Temperature dependent fit of the diffusion coefficient with respect to the driving force, the transport number with respect to the solvent, and the thermodynamic enhancement factor for LiPF<sub>6</sub> in EC:DEC, with T<sub>ref</sub> = 25 °C.

The fits are not perfect, but still provide useful information when modeling the temperature dependent behavior of batteries, as very few studies of this temperature dependency exist.

### 3.1.4 Electrochemical stability

The negative electrode in a LIB is highly reductive, with potentials of around -3 V vs the standard hydrogen electrode. This creates problems for the electrolyte components which can be reduced at the negative electrode. In a LIB the electrolyte is stabilized by a passivating layer formed during the first cycles, called the SEI. The ability to form a stable SEI, along with issues with other solvents co-intercalating into graphite, is why organic carbonates are used in practically all LIBs. However, salt superconcentration has been shown to overcome these issues for other organic solvents, and it is therefore of utmost importance to study the electrochemical stability when looking at these electrolytes. This is done

by cyclic voltammograms, as seen in Figure 19 for LiTFSI in ACN from Paper III. It can be seen that the electrochemical stability increases with concentration up to 3.6 M, when it can be considered as stable, also suggesting that it is the concentration at which it can be considered to have superconcentrated properties.

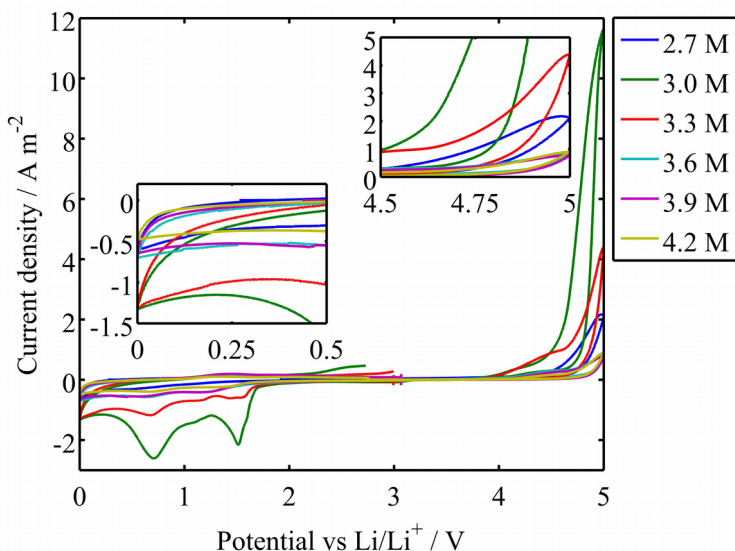


**Figure 19:** Cyclic voltammograms for a stainless steel/Li-foil cell between 0 and 5 V vs  $\text{Li}/\text{Li}^+$  for LiTFSI in ACN for different LiTFSI concentrations at 25 °C using a scan rate of 1 mV/s.

### 3.1.5 Electrolyte benchmarking using electrolyte mass transport resistivity

Benchmarking of LIB electrolytes is commonly done by measuring the ionic conductivity, giving an incomplete picture of the electrolyte performance. This is because of its relative simplicity and speed, since full characterizations based on concentrated electrolyte theory are still quite time-consuming and complicated. This is the background to the introduction of the benchmarking method termed EMTR, a relatively quick and simple method introduced by Nyman *et al.*<sup>90,102</sup>, providing measures of the polarization related to all mass transport limitations in the electrolyte at steady state, i.e. both ohmic and concentration polarization. It has a theoretical background in concentrated electrolyte theory, as seen in Equation 10 for a binary electrolyte in one solvent, but can be experimentally determined by measuring the ionic conductivity (providing the ohmic resistivity) and a galvanostatic polarization experiment (providing the diffusion resistivity), see Figures 1 and 2, then using Equation 29:

$$-\frac{(\partial \Phi / \partial x)_{S.S.}}{i} = \frac{1}{\kappa} + \frac{\Delta \Phi_{diff,S.S.}}{L} \cdot \frac{1}{i} \cdot \varepsilon^\beta \quad (29)$$

Figure 20 shows the EMTR for LiPF<sub>6</sub> in EC:DEC, LiTFSI in EmimTFSI:EC, LiTFSI in ACN, LiTf in PEO, LiPF<sub>6</sub> in PVdF-co-HFP and EC:PC, and LiPF<sub>6</sub> and TPP in EC:DEC, determined by experimental methods, as in Paper I and IV. It can be seen that the ratio between the diffusion and the ohmic resistivity is very different for the different systems, but for all systems except the superconcentrated electrolyte at its highest concentration, the diffusion resistivity is dominating, showing how misleading ionic conductivity (i.e. ohmic resistivity) alone can be.

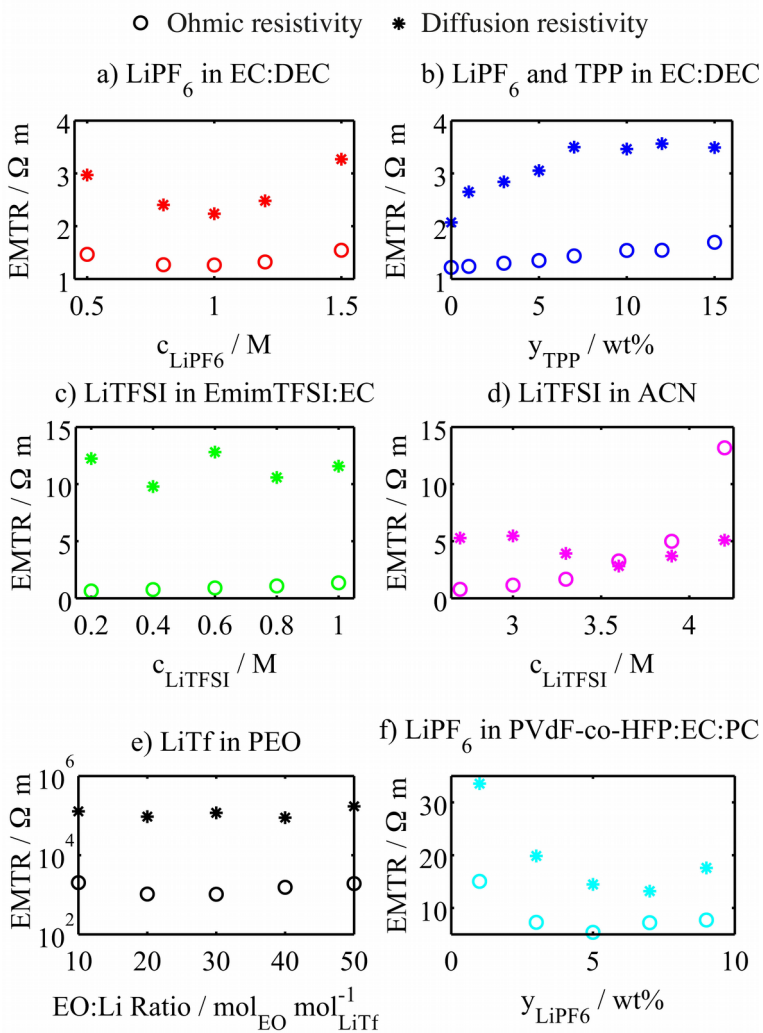


**Figure 20:** Experimentally determined electrolyte mass transport resistivity (EMTR) at 25 °C for a) LiPF<sub>6</sub> in EC:DEC b) LiPF<sub>6</sub> and TPP in EC:DEC c) LiTFSI in EmimTFSI:EC d) LiTFSI in ACN e) LiTf in PEO f) LiPF<sub>6</sub> in PVdF-co-HFP and EC:PC.

### 3.2 TPP Flame retardant in HEV application

When testing full cells it is important to use relevant tests for the intended application, as the way the batteries will be used is very different for different applications. To simulate the environment of HEV batteries, HPPC tests were developed. They are highly dynamic and consist of short high-current pulses emulating the behavior of HEVs. In Paper I, the charge-neutral HPPC cycle EUCAR was used to evaluate if the flame retardant TPP was suitable for HEV applications<sup>88</sup>. Pouch cells were assembled with power optimized graphite/LiFePO<sub>4</sub> electrodes, ensuring high capabilities. Figure 21 shows the cell potential during a EUCAR cycle with different amounts of TPP added to a base electrolyte with 1 M LiPF<sub>6</sub> in EC:DEC.

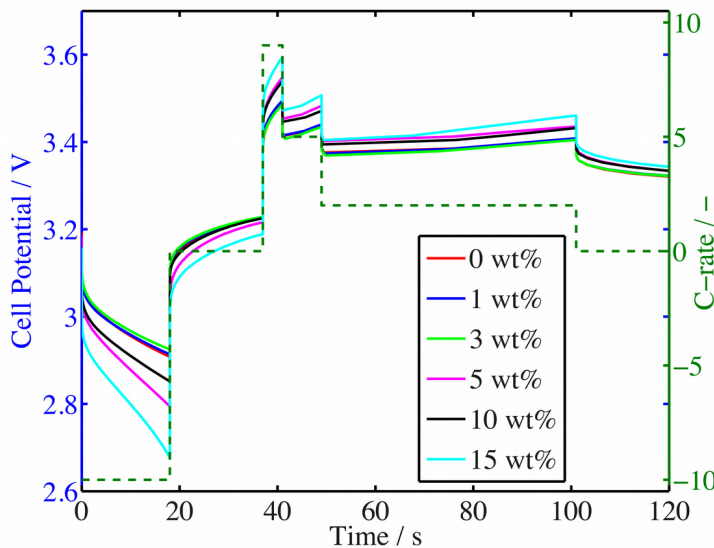


**Figure 21:** Cell potential and C-rates during EUCAR cycle for graphite|LiPF<sub>6</sub> in EC:DEC| LiFePO<sub>4</sub> cell with different amounts of TPP.

The polarization increases steadily with increasing TPP amounts above ~3 wt%, meaning that less and less useful energy will be generated. Another highly relevant parameter when evaluating a flame retardant is

its flame retarding capabilities, obviously. Table 4 shows the self-extinguishing time and flash point, as well as the energy efficiency for the EUCAR cycle from Figure 21 (i.e. energy generated during discharge divided by the energy needed for charging), for different TPP amounts.

**Table 4:** Self-extinguishing time, flash-point and EUCAR energy efficiency for LiPF<sub>6</sub> in EC:DEC with different amounts of TPP.

TPP content / wt%	Self-extinguishing time / s g <sup>-1</sup>	Flash point / °C	EUCAR energy efficiency / %
0	62.0 ( $\pm$ 5)	36.0	87.4
1	61.5 ( $\pm$ 2)	36.9	87.1
3	58.0 ( $\pm$ 4)	36.4	87.5
5	59.0 ( $\pm$ 7)	37.4	83.6
10	51.5 ( $\pm$ 5)	37.0	84.6
15	50.5 ( $\pm$ 6)	No data	80.7

Even though the self-extinguishing time decreases from 62 s g<sup>-1</sup> to  $\sim$ 50 s g<sup>-1</sup>, the reduction is too small to be considered a “flame-retarded electrolyte” and even larger amounts are needed to achieve the desired effect. The addition of TPP has an insignificant effect on the flash point as expected, which is constant at around 36 °C, since the flash point is mainly dependent on the vapor phase composition, which is not altered much. The energy efficiency, however, changes quite a lot, dropping by almost 8%, from 87.4 % to 80.7 %. Summing up all of these effects, this additive is not considered suitable for HEV applications since it does not improve safety significantly but decreases the electrochemical performance greatly.

### 3.3 Thermal modeling of commercial 25 Ah battery in PHEV application

Electrochemical models coupled with thermal models are very useful engineering tools to evaluate e.g. battery/module/pack design, thermal management strategies, and the limiting processes within the battery.

#### 3.4.1 Model validation

To fully trust the results of models, validation is important. The model used in Paper V was validated using both cell potential (Figure 22, also showing applied C-rates) and battery cell exterior surface temperature data (Figure 23, probe locations in Figure 6). The simulated cell potential fits the data well. The model temperatures fit the experiments fair, but keep in mind that the case studied is very demanding, with very high currents.

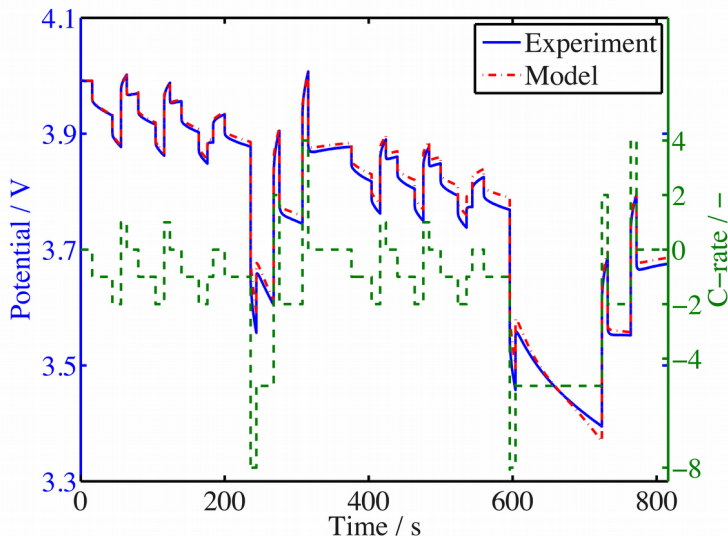


**Figure 22:** Simulated and experimental cell potentials and C-rates during ISO DDPP A and B for commercial 25 Ah graphite | NMC battery.

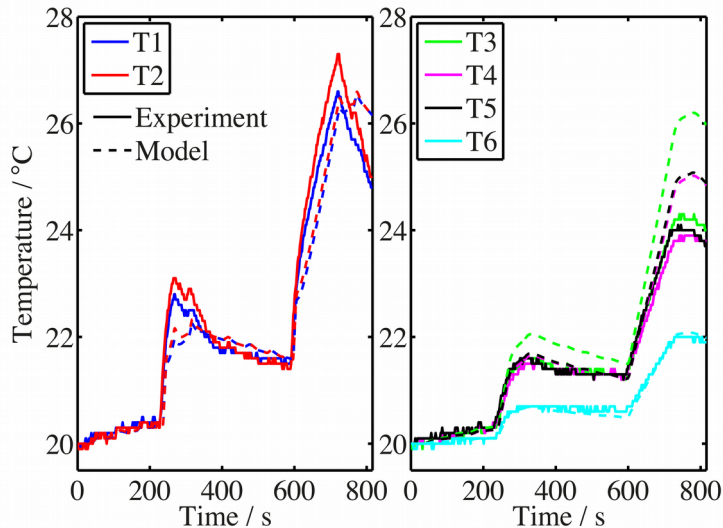


**Figure 23:** Simulated and experimental cell can surface temperatures during ISO DDPP A and B for commercial 25 Ah graphite | NMC battery.

### 3.4.2 Electrochemical processes and internal thermal performance

Cell can surface temperatures are normally used when studying thermal processes experimentally or validating thermal models since they are easily measured. However, the truly important information lies in the internal temperature where the electrochemical reactions take place. Figure 24 shows the maximum and minimum jellyroll temperature as functions of time and Figure 25 the internal temperature distribution at 724 s, right after the 120 s long 5 C (125 A) pulse. A notable feature when studying Figures 23 and 24 is that the temperature increases mainly during the high current pulses.

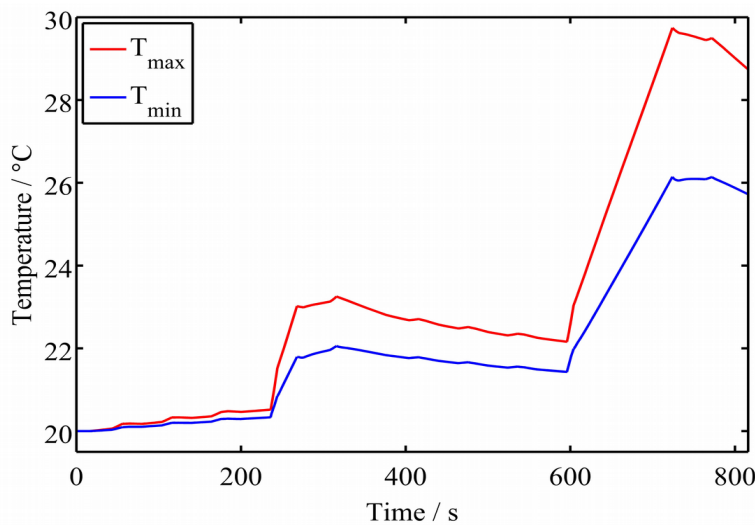


**Figure 24:** Maximum and minimum jellyroll temperatures.

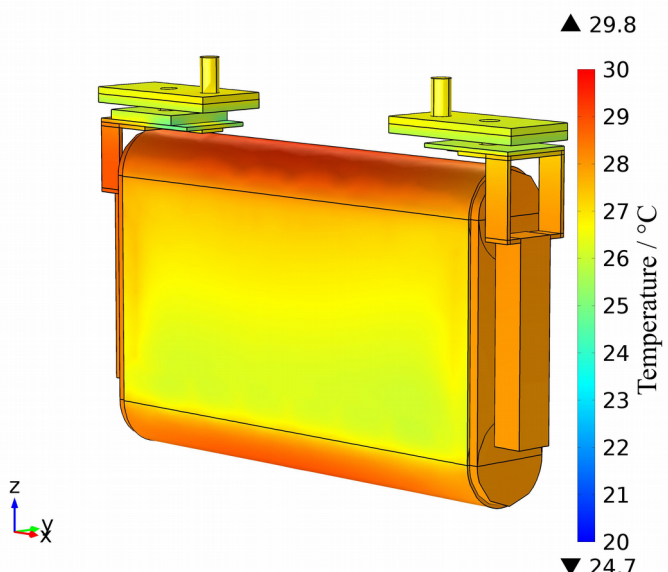


**Figure 25:** Internal temperature distribution at 724 s.

The temperature of the jellyroll is highest at the center, see Figure 26. This observed temperature distribution will have serious long-term effects, and can probably explain the non-uniform aging observed by Klett *et al.*, who observed increased aging in the core of the jellyroll in a cylindrical cell<sup>109</sup>.

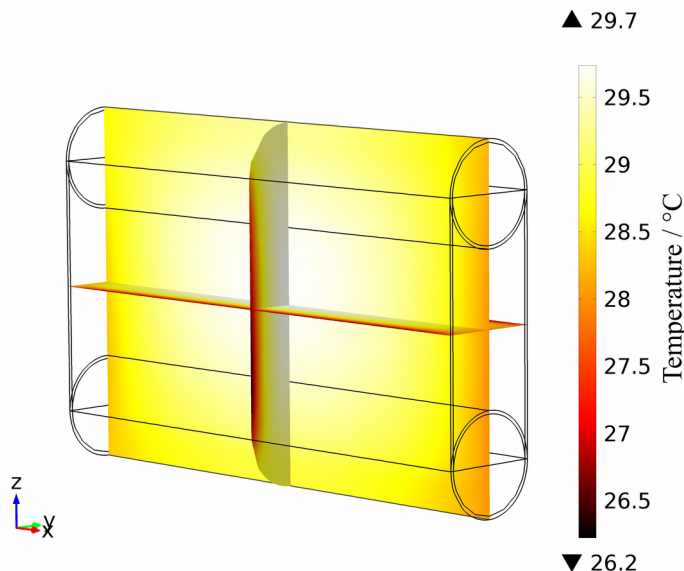


**Figure 26:** Cross section of temperature distribution at 724 s for the jellyroll.

One of the main limiting processes within the battery was found to be the electrolyte concentration, as seen in Figure 27, which reaches extreme values at both electrodes during the high current pulses. This leads to a very uneven current distribution, and large polarizations.

Additionally, different thermal management strategies were evaluated by changing the surface that was connected to the heat sink. However, this had little impact on the temperature of the jellyroll. This is simply because the heat transfer limitations lie in the jellyroll, and not in the battery cell exterior.

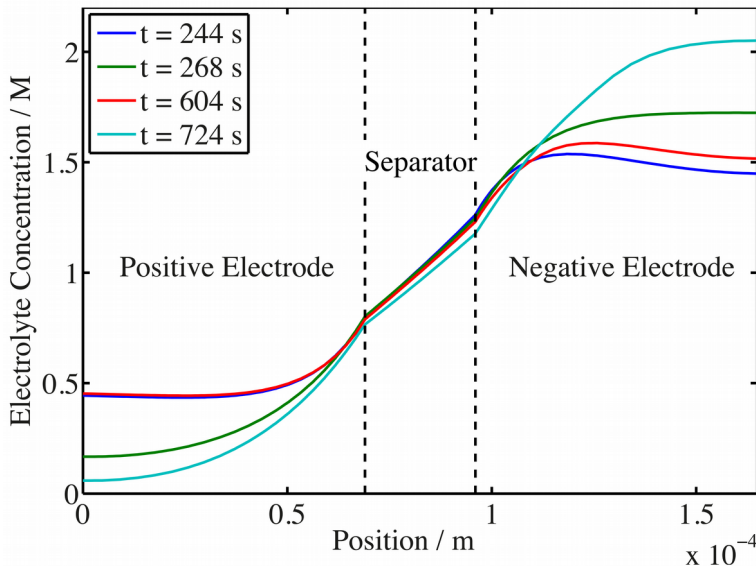


**Figure 27:** Simulated electrolyte concentrations at selected times during ISO DDPP A and B.

### 3.4.3 Comparison using different electrolytes

To illustrate the importance of the electrolyte, and electrolyte mass transport characterizations, simulations with the electrolyte properties determined in Papers II and III were made, using initial concentrations of 1.0 M and 3.6 M, respectively. Both electrolytes were assumed to have the temperature dependency determined in Section 3.1 in this thesis. A comparison of the cell potentials during the cycling scheme used in Paper V can be seen in Figure 28. The base electrolyte, LiPF<sub>6</sub> in EC:EMC (3:7, by weight), greatly outperforms the other two electrolytes, showing that they are not suitable for high-power applications.

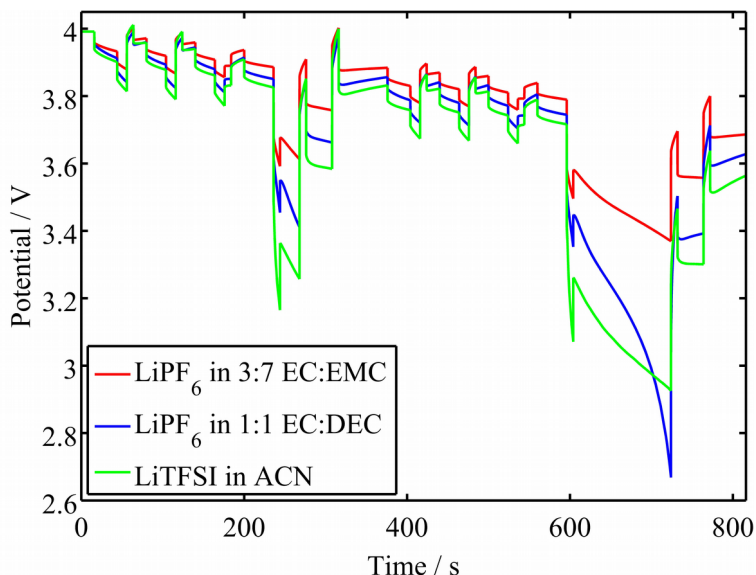


**Figure 28:** Simulated cell potentials during ISO DDPP A and B with different electrolytes.

Simulations also showed that both LiPF<sub>6</sub> in EC:DEC (1:1, by weight) and LiTFSI in ACN reach higher concentrations than physically possible during the high current current pulses, 2.36 M (solvation limit ~ 1.75 M) and 6.55 M (solvation limit ~ 4.5 M), respectively, assuming that the transport properties have a constant value outside their defined intervals. This obviously has a huge effect, and yields results that cannot entirely be trusted. However, that effect would only make them perform even worse in real life or in a model considering those effects, as salt precipitation would block the pores and prevent mass transport. The reason why LiPF<sub>6</sub> in EC:DEC shows extremely high polarization during the 120 s long 5 C pulse is because the electrolyte concentration reaches close to zero for larger and larger parts of the positive electrode. The superconcentrated electrolyte does not exhibit this behavior, since it has such a high initial concentration. For LiTFSI in ACN, the concentration difference in the electrolyte reaches 6.5 M at 724 s, an impossibly high value.



## Chapter 4: Future work

One very interesting study would be to use the detailed thermal model to study aging effects. To do this the electrochemical model would need to be simplified significantly or possibly be exchanged for something less complicated.

As any study will be very dependent on its input, to characterize the materials (e.g. electrodes, electrolyte, plastic components) of the battery used in Paper V would be very helpful, especially for the electrochemical model. Although the fit was fairly good even with the assumed parameters, characterizing the actual materials would be very beneficial, and would also be valuable for other researchers with very different research topics, such as materials science, as well as for modeling purposes.

The electrochemical techniques used in Papers I-IV, except for the full-cell cycling in Paper I, all use lithium metal electrodes. This has inherent problems, as most solvents are not stable at its operating potential, and a mixed potential may be recorded. To find an alternative electrode operating at a different potential, or develop alternative methods not requiring lithium metal electrodes, would be extremely beneficial.

To perform a full characterization of an electrolyte containing all the additives present in a commercial LIB and over a wide temperature range (e.g. the -30 °C to + 52 °C suggested by the PNGV) would provide very useful information, since it would be closer to the final product and over the entire operating temperature range.



## Chapter 5: Conclusions

The full electrolyte mass transport characterization of Nyman et al. was successfully expanded to include temperature dependence. All studied properties were found to vary highly with temperature and concentration. The superconcentrated electrolyte with LiTFSI in ACN was found to have very different mass transport properties compared to conventional LIB electrolytes. A notable difference is stronger and stronger interactions between the solvent and the anion with increasing salt concentrations leading to very high lithium-ion transport numbers, opposite behavior of organic carbonate electrolytes. Partial molar volumes showed just how bulky LiTFSI is compared to the more commonly used LiPF<sub>6</sub>, with a partial molar volume more than twice as big (142 vs 61 cm<sup>3</sup> mol<sup>-1</sup>). Changes in ionic conductivity and diffusion coefficient were found to be mostly due to viscosity changes.

Electrolyte mass transport resistivity was successfully used to benchmark the mass transport limitations at steady state of several systems, including organic-solvent based electrolytes, ionic liquids, solid polymers, gelled polymers, and electrolytes containing flame retardant additives. The systems were found to have very different performance, but overall diffusion resistivity was found to be the dominating polarization source for all systems except at the highest concentrations for the superconcentrated electrolyte.

New temperature dependent fits of the mass transport properties of LiPF<sub>6</sub> in EC:DEC were calculated, easier to implement in thermal models but with slightly worse fit.

The flame retardant electrolyte additive TPP was evaluated for a HEV application using the EUCAR cycle and was found to be unsuitable for such applications, as the benefit from a decreased flammability is lower than the decrease in the electrochemical performance.

A coupled electrochemical/thermal model was used to evaluate the design and thermal management of a commercial 25 Ah battery connected to a heat sink in a PHEV application using COMSOL Multiphysics. The model

was successfully validated using cell potential and surface temperature data. Different thermal management strategies were evaluated and found to have very little effect on the jellyroll temperature distribution. Clearly, what surface to cool is not the limiting factor for the thermal design of large-format batteries and their thermal management systems.

The effect of switching the electrolyte in the coupled electrochemical and thermal model of Paper V from LiPF<sub>6</sub> in EC:EMC to LiPF<sub>6</sub> in EC:DEC or LiTFSI in ACN was illustrated, using the determined properties from Papers II and III. Both electrolytes were found to have very poor performance, reached physically impossible concentrations which would result in salt precipitation, and proved unsuitable for the demanding load cycle used.

## Chapter 6: List of symbols

$1 + \frac{\partial \ln f_{\pm}}{\partial \ln c_{salt}}$	Thermodynamic enhancement factor
$A$	Area
$\hat{A}$	Specific area
$c_j$	Concentration of species j
$C_p$	Heat capacity at constant pressure
$\tilde{D}_{salt}$	Thermodynamic diffusion coefficient
$D_{App}$	Apparent diffusion coefficient
$E_a$	Activation energy
$F$	Faraday's constant
$i$	Current density
$i_0$	Exchange current density
$i_{tot}$	Volumetric electrochemical reaction current source
$k$	Thermal conductivity
$L$	Length of cell / Electrolyte thickness
$N_-$	Anion flux
$Q$	Heat generation rate
$R_{electrolyte}$	Electrolyte resistance
$R$	Ideal gas constant
$t$	Time
$t_+^{solv}$	$\text{Li}^+$ transport number with respect to the solvent
$t_+$	$\text{Li}^+$ transport number with respect to the room
$T$	Temperature
$V_m^j$	Molar volume of species j
$W$	Walden product
$y_j$	Weight fraction of species j

## Greek letters

$\alpha_i$	Electrochemical reaction symmetry factor
$\beta$	Bruggeman coefficient
$\varepsilon$	Volume fraction
$\eta$	Overpotential
$\kappa$	Ionic conductivity
$\Lambda$	Limiting molar conductivity
$\mu$	Dynamic viscosity
$\rho$	Density
$\sigma_s$	Electronic conductivity
$\tau$	Dimensionless time
$\Phi$	Electric potential

## Subscripts

$_L$	Electrolyte
$_S$	Solid phase
$_{salt}$	Salt (LiPF <sub>6</sub> or LiTFSI)
$_{solv}$	Solvent (EC:DEC or ACN)

## Chapter 7: Acknowledgements

The Swedish Hybrid Vehicle Centre (SHC) is gratefully acknowledged for the funding.

To my supervisors, Göran Lindbergh and Mårten Behm, who have been supportive, inspirational, and good at brainstorming ideas with!

To all my collaborators: Tommy, Kasia, Susanne, Henrik, Pontus, and Carl. I hope that there will be more opportunities to collaborate in the future!

To my present and former colleagues at TEK. Thank you for all the interesting, and sarcastic discussions in the lunch room! A special thanks to the PhD student colleagues that I have had the pleasure to travel abroad with: Jonas, Matilda, Verena, Maria, Pontus and Simon. It has been extremely fun! A very special thanks to Tommy for hosting our very own homebrewery. It has been a great way to stay in contact in the life after KTH.

Till min Åsa, som har varit ett stort stöd genom hela min tid som doktorand (och innan). Jag är så glad att vi har varandra! <3

Till min familj. Mamma Siv, pappa Roland, Åsa, Petra, Fredrik, Sebastian, Marre, Ingall, Roffe och Sofia – Ni är bäst!

Till mina närmsta vänner. Pelle, Oskar, Viktor, Alex, Johannes, Jonatan, Mathias, Andreas och Philip – Rock on! Jag förväntar mig många ölkällor framöver.

Till grabbgänget från kemi på KTH. Andreas, Philip, CP Orsch, Bruce, Mackan, Börje, Blake, Rufus och Tobbe. Utan er hade de här 10 åren på KTH varit otroligt tråkiga!

To my American (and Nigerian) friends. Alec, Adam, and Jide. I am so glad that we still stay in contact and see each other. I only wish we could meet up more often!



## Chapter 8: References

- (1) Scrosati, B.; Garche, J. *J. Power Sources* **2010**, *195*, 2419–2430.
- (2) Global Battery Markets  
[http://batteryuniversity.com/learn/article/global\\_battery\\_markets](http://batteryuniversity.com/learn/article/global_battery_markets) (accessed Apr 20, 2015).
- (3) Lithium-ion battery market estimation  
<http://www.statista.com/statistics/309579/lithium-ion-battery-market-estimation/> (accessed Apr 20, 2015).
- (4) Armand, M.; Tarascon, J.-M. *Nature* **2008**, *451*, 652–657.
- (5) Bruce, P. G.; Freunberger, S. a.; Hardwick, L. J.; Tarascon, J.-M. *Nat. Mater.* **2011**, *11*, 172–172.
- (6) Whittingham, M. S. *Science (80-)* **1976**, *192*, 1126–1127.
- (7) Whittingham, M. S.; Gamble, F. R. *Mater. Res. Bull.* **1975**, *10*, 363–371.
- (8) Whittingham, M. S. *Proc. IEEE* **2012**, *100*, 1518–1534.
- (9) Besenhard, J. O. *Carbon N. Y.* **1976**, *14*, 111–115.
- (10) Besenhard, J. O.; Fritz, H. P. *J. Electroanal. Chem. Interfacial Electrochem.* **1974**, *53*, 329–333.
- (11) Tarascon, J.-M.; Armand, M. *Nature* **2001**, *414*, 359–367.
- (12) Bandhauer, T. M.; Garimella, S.; Fuller, T. F. *J. Electrochem. Soc.* **2011**, *158*, R1.
- (13) Idaho Operations Office. *Battery Test Manual For Plug-In Hybrid Electric Vehicles*; 2008.
- (14) Broussely, M.; Biensan, P.; Bonhomme, F.; Blanchard, P.; Herreyre, S.; Nechev, K.; Staniewicz, R. *J. Power Sources* **2005**, *146*, 90–96.
- (15) Fan, J.; Tan, S. *J. Electrochem. Soc.* **2006**, *153*, A1081.
- (16) Amine, K.; Liu, J.; Belharouak, I. *Electrochim. commun.* **2005**, *7*, 669–673.
- (17) Safari, M.; Delacourt, C. *J. Electrochem. Soc.* **2011**, *158*, A1123.
- (18) Ekström, H.; Lindbergh, G. *J. Electrochem. Soc.* **2015**, *162*, A1003–

- A1007.
- (19) Kassem, M.; Bernard, J.; Revel, R.; Pélissier, S.; Duclaud, F.; Delacourt, C. *J. Power Sources* **2012**, *217*, 574.
- (20) Fan, L.; Khodadadi, J. M.; Pesaran, a. a. *J. Power Sources* **2013**, *238*, 301–312.
- (21) Xun, J.; Liu, R.; Jiao, K. *J. Power Sources* **2013**, *233*, 47–61.
- (22) Park, H. *J. Power Sources* **2013**, *239*, 30–36.
- (23) Zhang, X.; Kong, X.; Li, G.; Li, J. *Energy* **2014**, *64*, 1092–1101.
- (24) Bandhauer, T. M.; Garimella, S.; Fuller, T. F. *J. Electrochem. Soc.* **2015**, *162*, 0–11.
- (25) Al-Hallaj, S.; Selman, J. R. *J. Power Sources* **2002**, *110*, 341–348.
- (26) Kizilel, R.; Sabbah, R.; Selman, J. R.; Al-Hallaj, S. *J. Power Sources* **2009**, *194*, 1105–1112.
- (27) Sabbah, R.; Kizilel, R.; Selman, J. R.; Al-Hallaj, S. *J. Power Sources* **2008**, *182*, 630–638.
- (28) Rao, Z.; Wang, S. *Renew. Sustain. Energy Rev.* **2011**, *15*, 4554–4571.
- (29) Reddy, T. *Linden's handbook of batteries*; 4th ed.; McGraw-Hill Professional, 2010.
- (30) Valøen, L. O.; Reimers, J. N. *J. Electrochem. Soc.* **2005**, *152*, A882.
- (31) Lundgren, H.; Behm, M.; Lindbergh, G. *J. Electrochem. Soc.* **2015**, *162*, A413–A420.
- (32) Bernardi, D.; Pawlikowski, E.; Newman, J. *J. Electrochem. Soc.* **1985**, *132*, 5.
- (33) Chen, Y.; Evans, J. W. *J. Electrochem. Soc.* **1993**, *140*, 1833–1838.
- (34) Pals, C. R.; Newman, J. *J. Electrochem. Soc.* **1995**, *142*, 3274–3281.
- (35) Pals, C. R.; Newman, J. *J. Electrochem. Soc.* **1995**, *142*, 3282–3288.
- (36) Rao, L.; Newman, J. *J. Electrochem. Soc.* **1997**, *144*, 2697.
- (37) Botte, G. G. *J. Electrochem. Soc.* **1999**, *146*, 914.
- (38) Song, L.; Evans, J. W. *J. Electrochem. Soc.* **2000**, *147*, 2086–2095.
- (39) Gu, W. B.; Wang, C. *J. Electrochem. Soc.* **2000**, *147*, 2910–2922.

- (40) Srinivasan, V.; Wang, C. *J. Electrochem. Soc.* **2003**, *150*, A98.
- (41) Thomas, K. E.; Newman, J. *J. Electrochem. Soc.* **2003**, *150*, A176–A192.
- (42) Chen, S.-C.; Wan, C.-C.; Wang, Y.-Y. *J. Power Sources* **2005**, *140*, 111–124.
- (43) Kumaresan, K.; Sikha, G.; White, R. E. *J. Electrochem. Soc.* **2008**, *155*, A164.
- (44) Guo, M.; White, R. E. *J. Electrochem. Soc.* **2011**, *158*, A1166.
- (45) Zavalis, T. G.; Behm, M.; Lindbergh, G. *J. Electrochem. Soc.* **2012**, *159*, A848.
- (46) Guo, M.; White, R. E. *J. Power Sources* **2013**, *221*, 334–344.
- (47) Mao, J.; Tiedemann, W.; Newman, J. *J. Power Sources* **2014**, *271*, 444–454.
- (48) Verbrugge, M. W.; Conell, R. S. *J. Electrochem. Soc.* **2002**, *149*, A45.
- (49) Dubarry, M.; Vuillaume, N.; Liaw, B. Y. *J. Power Sources* **2009**, *186*, 500–507.
- (50) Onda, K.; Ohshima, T.; Nakayama, M.; Fukuda, K.; Araki, T. *J. Power Sources* **2006**, *158*, 535–542.
- (51) Chacko, S.; Chung, Y. M. *J. Power Sources* **2012**, *213*, 296–303.
- (52) Goodenough, J. B.; Kim, Y. *Chem. Mater.* **2010**, *22*, 587–603.
- (53) Balakrishnan, P. G.; Ramesh, R.; Prem Kumar, T. *J. Power Sources* **2006**, *155*, 401–414.
- (54) Chung, G.-C.; Kim, H.-J.; Yu, S.-I.; Jun, S.-H.; Choi, J.; Kim, M.-H. *J. Electrochem. Soc.* **2000**, *147*, 4391.
- (55) Abe, T.; Fukuda, H.; Iriyama, Y.; Ogumi, Z. *J. Electrochem. Soc.* **2004**, *151*, A1120.
- (56) Abe, T.; Kawabata, N.; Mizutani, Y.; Inaba, M.; Ogumi, Z. *J. Electrochem. Soc.* **2003**, *150*, A257.
- (57) Von Wald Cresce, A.; Borodin, O.; Xu, K. *J. Phys. Chem. C* **2012**, *116*, 26111–26117.
- (58) Seo, D. M.; Borodin, O.; Han, S.-D.; Ly, Q.; Boyle, P. D.; Henderson, W. a. *J. Electrochem. Soc.* **2012**, *159*, A1489.

58 | Chapter 8: References

- (59) Seo, D. M.; Borodin, O.; Han, S.-D.; Ly, Q.; Boyle, P. D.; Henderson, W. a. *J. Electrochem. Soc.* **2012**, *159*, A553.
- (60) Yamada, Y.; Yaegashi, M.; Abe, T.; Yamada, A. *Chem. Commun.* **2013**, *49*, 11194–11196.
- (61) Yamada, Y.; Furukawa, K.; Sodeyama, K.; Kikuchi, K.; Yaegashi, M.; Tateyama, Y.; Yamada, A. *J. Am. Chem. Soc.* **2014**, *136*, 5039–5046.
- (62) Yamada, Y.; Takazawa, Y.; Miyazaki, K.; Abe, T. *J. Phys. Chem. C* **2010**, *114*, 11680–11685.
- (63) Sodeyama, K.; Yamada, Y.; Aikawa, K.; Yamada, A.; Tateyama, Y. *J. Phys. Chem. C* **2014**, *118*, 14091–14097.
- (64) Yamada, Y.; Usui, K.; Chiang, C. H.; Kikuchi, K.; Furukawa, K.; Yamada, A. *ACS Appl. Mater. Interfaces* **2014**, *6*, 10892–10899.
- (65) Suo, L.; Hu, Y.-S.; Li, H.; Armand, M.; Chen, L. *Nat. Commun.* **2013**, *4*, 1481.
- (66) *Interim Factual Report - Auxiliary Power Unit Battery Fire Japan Airlines Boeing 787-8, JA829J*; Boston, Massachusetts, 2013.
- (67) Wang, H.; Tang, a; Huang, K. *Chinese J. Chem.* **2011**, *1583–1588*.
- (68) Jansen, a. ; Kahaian, a. ; Kepler, K. .; Nelson, P. .; Amine, K.; Dees, D. .; Vissers, D. .; Thackeray, M. . *J. Power Sources* **1999**, *81-82*, 902–905.
- (69) Xu, K. *Chem. Rev.* **2004**, *104*, 4303–4417.
- (70) Spotnitz, R.; Franklin, J. *J. Power Sources* **2003**, *113*, 81–100.
- (71) Abraham, D. P.; Roth, E. P.; Kostecki, R.; McCarthy, K.; MacLaren, S.; Doughty, D. H. *J. Power Sources* **2006**, *161*, 648–657.
- (72) Nakagawa, H.; Fujino, Y.; Kozono, S.; Katayama, Y.; Nukuda, T.; Sakaebe, H.; Matsumoto, H.; Tatsumi, K. *J. Power Sources* **2007**, *174*, 1021–1026.
- (73) Kim, G. T.; Jeong, S. S.; Joost, M.; Rocca, E.; Winter, M.; Passerini, S.; Balducci, A. *J. Power Sources* **2011**, *196*, 2187–2194.
- (74) Mizuno, F.; Hayashi, a.; Tadanaga, K.; Tatsumisago, M. *Adv. Mater.* **2005**, *17*, 918–921.
- (75) Zhang, S. S. *J. Power Sources* **2006**, *162*, 1379–1394.

- (76) Wang, X.; Yasukawa, E.; Kasuya, S. *J. Electrochem. Soc.* **2001**, *148*, A1066.
- (77) Wang, X.; Yasukawa, E.; Kasuya, S. *J. Electrochem. Soc.* **2001**, *148*, A1058.
- (78) Xu, K.; Ding, M. S.; Zhang, S.; Allen, J. L.; Jow, T. R. *J. Electrochem. Soc.* **2002**, *149*, A622.
- (79) Wang, Q.; Sun, J.; Yao, X.; Chen, C. *Electrochim. Solid-State Lett.* **2005**, *8*, A467.
- (80) Hyung, Y. E.; Vissers, D. R.; Amine, K. *J. Power Sources* **2003**, *119–121*, 383–387.
- (81) Green, J. *J. Fire Sci.* **1992**, *10*, 470–487.
- (82) Granzow, A. *Acc. Chem. Res.* **1978**, *11*, 177–183.
- (83) Dunn, R. P.; Kafle, J.; Krause, F. C.; Hwang, C.; Ratnakumar, B. V.; Smart, M. C.; Lucht, B. L. *J. Electrochem. Soc.* **2012**, *159*, A2100–A2108.
- (84) Shim, E.-G.; Nam, T.-H.; Kim, J.-G.; Kim, H.-S.; Moon, S.-I. *J. Power Sources* **2007**, *172*, 919–924.
- (85) Shim, E.-G.; Nam, T.-H.; Kim, J.-G.; Kim, H.-S.; Moon, S.-I. *J. Power Sources* **2007**, *172*, 901–907.
- (86) Ping, P.; Wang, Q. S.; Sun, J. H.; Xia, X.; Dahn, J. R. *J. Electrochem. Soc.* **2012**, *159*, A1467–A1473.
- (87) Xia, X.; Ping, P.; Dahn, J. R. *J. Electrochem. Soc.* **2012**, *159*, A1460–A1466.
- (88) EUCAR: *Traction Battery Working Group, Specification of Test Procedures for Hybrid Electric Vehicle Traction Batteries*; 1998.
- (89) *Electrically Propelled Road Vehicles - Test Specifications for Lithium-ion Traction Battery Packs and Systems - Part 2: High energy application, ISO 12405-2*; 2010; Vol. 7.
- (90) Nyman, A.; Behm, M.; Lindbergh, G. *Electrochim. Acta* **2008**, *53*, 6356–6365.
- (91) Doyle, M.; Fuller, T. F.; Newman, J. *J. Electrochem. Soc.* **1993**, *140*, 1526–1533.
- (92) Fuller, T. F.; Doyle, M.; Newman, J. *J. Electrochem. Soc.* **1994**, *141*, 1–10.

- (93) Fuller, T. F.; Doyle, M.; Newman, J. *J. Electrochem. Soc.* **1994**, *141*, 982.
- (94) Newman, J.; Thomas-Alyea, K. E. *Electrochemical Systems*; 3rd ed.; John Wiley & Sons, 2004.
- (95) Newman, J.; Thomas, K. E.; Hafezi, H.; Wheeler, D. R. *J. Power Sources* **2003**, *119-121*, 838–843.
- (96) Wheeler, D. R.; Newman, J. *J. Phys. Chem. B* **2004**, *108*, 18353–18361.
- (97) Ma, Y.; Doyle, M.; Fuller, T. F.; Doeff, M. M.; De Jonghe, L. C.; Newman, J. *J. Electrochem. Soc.* **1995**, *142*, 1859–1868.
- (98) Doeff, M. M.; Geor  n, P.; Qiao, J.; Kerr, J.; Jonghe, L. C. *De J. Electrochem. Soc.* **1999**, *146*, 2024–2028.
- (99) Doeff, M. M.; Edman, L.; Sloop, S. E.; Kerr, J.; De Jonghe, L. C. *J. Power Sources* **2000**, *89*, 227–231.
- (100) Geor  n, P.; Lindbergh, G. *Electrochim. Acta* **2001**, *47*, 577–587.
- (101) Nyman, A.; Behm, M.; Lindbergh, G. *J. Electrochem. Soc.* **2011**, *158*, A628.
- (102) Nyman, A.; Behm, M.; Lindbergh, G. *J. Electrochem. Soc.* **2011**, *158*, A636.
- (103) Geor  n, P.; Lindbergh, G. *Electrochim. Acta* **2004**, *49*, 3497–3505.
- (104) Stewart, S. G.; Newman, J. *J. Electrochem. Soc.* **2008**, *155*, F13.
- (105) Stewart, S.; Newman, J. *J. Electrochem. Soc.* **2008**, *155*, A458.
- (106) Klett, M.; Giesecke, M.; Nyman, A.; Hallberg, F.; Wreland Lindstr  m, R.; Lindbergh, G.; Furo, I. *J. Am. Chem. Soc.* **2012**, *134*, 14654–14657.
- (107) Geor  n, P.; Adebahr, J.; Jacobsson, P.; Lindbergh, G. *J. Electrochem. Soc.* **2002**, *149*, A1015–A1019.
- (108) Ding, M. S.; Xu, K.; Zhang, S. S.; Amine, K.; Henriksen, G. L.; Jow, T. R. *J. Electrochem. Soc.* **2001**, *148*, A1196.
- (109) Klett, M.; Eriksson, R.; Groot, J.; Svens, P.; Ciosek H  gstr  m, K.; Lindstr  m, R. W.; Berg, H.; Gustafson, T.; Lindbergh, G.; Edstr  m, K. *J. Power Sources* **2014**, *257*, 126–137.